



# HHS Public Access

Author manuscript

*Cell Stem Cell*. Author manuscript; available in PMC 2024 November 02.

Published in final edited form as:

*Cell Stem Cell*. 2023 November 02; 30(11): 1472–1485.e7. doi:10.1016/j.stem.2023.09.012.

## Skull progenitor cell-driven meningeal lymphatic restoration improves neurocognitive functions in craniosynostosis

Li Ma<sup>1,#</sup>, Qing Chang<sup>1,#</sup>, Fei Pei<sup>1</sup>, Mengmeng Liu<sup>1</sup>, Wei Zhang<sup>1</sup>, Young-Kwon Hong<sup>2</sup>, Yang Chai<sup>1,\*</sup>, Jian-Fu Chen<sup>1,3,\*</sup>

<sup>1</sup>Center for Craniofacial Molecular Biology, University of Southern California, Los Angeles, CA 90033, USA

<sup>2</sup>Department of Surgery, Norris Comprehensive Cancer Center, Keck School of Medicine of USC, Los Angeles, CA 90033, USA

<sup>3</sup>Lead contact

### SUMMARY

The meninges lie in the interface between the skull and brain, harboring lymphatic vasculature and skull progenitor cells (SPCs). How the skull and brain communicate remains largely unknown. We found that impaired meningeal lymphatics and brain perfusion drive neurocognitive defects in *Twist1*<sup>+/-</sup> mice, an animal model of craniosynostosis recapitulating human Saethre-Chotzen syndrome. Loss of SPCs leads to skull deformities and elevated intracranial pressure (ICP), while transplanting SPCs back into mutant mice mitigates lymphatic and brain defects through two mechanisms: (i) decreasing elevated ICP by skull correction; and (ii) promoting the growth and migration of lymphatic endothelial cells (LECs) via SPC-secreted vascular endothelial growth factor-C (VEGF-C). Treating *Twist1*<sup>+/-</sup> mice with VEGF-C promotes meningeal lymphatic growth and rescues defects in ICP, brain perfusion, and neurocognitive functions. Thus, the skull functionally integrates with the brain via meningeal lymphatics, which is impaired in craniosynostosis and can be restored by SPC-driven lymphatic activation via VEGF-C.

### Graphical Abstract

\*Correspondence: ychai@usc.edu, Jianfu@usc.edu.

#These authors contributed equally to this work.

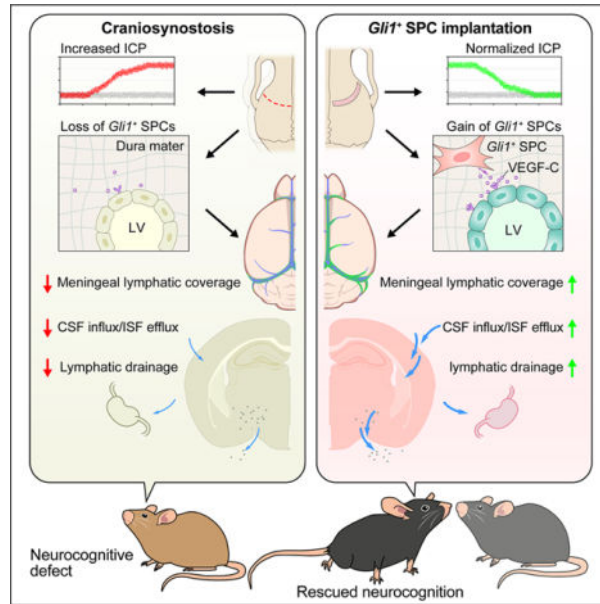
#### AUTHOR CONTRIBUTIONS

L.M., Q.C., M-M.L., F.P., W.Z conceived and performed all experiments. Y-K.H. helped with the manuscript writing. J-F.C., Y.C. and L.M designed and interpreted the experiments and wrote the manuscript.

**Publisher's Disclaimer:** This is a PDF file of an unedited manuscript that has been accepted for publication. As a service to our customers we are providing this early version of the manuscript. The manuscript will undergo copyediting, typesetting, and review of the resulting proof before it is published in its final form. Please note that during the production process errors may be discovered which could affect the content, and all legal disclaimers that apply to the journal pertain.

#### DECLARATION OF INTERESTS

The authors declare there are no competing financial interests that might be perceived as affecting the objectivity of these studies.



## In brief

Chen and colleagues found that the skull communicates with the brain through meningeal lymphatic vasculature. Skull progenitor cells directly support lymphatic vessel growth and can be exploited to activate brain lymphatic drainage functions as a therapeutic strategy for treating neurocognitive defects in craniosynostosis diseases.

## Keywords

Skull progenitor cells (SPCs); meningeal lymphatics; neurocognitive functions; mouse behaviors; craniosynostosis

## INTRODUCTION

The meninges lie between the skull (calvaria) and the brain and are composed of three layers: the dura, arachnoid, and pia maters<sup>1,2</sup>. The dura mater consists of two layers: the outermost layer is closely adherent to the underside of skull bones and forms the periosteum; the inner layer immediately contacts the arachnoid mater cells<sup>2,3</sup>. The dura mater contains skull progenitor cells (SPCs), which contribute to calvarial bone development, homeostasis, and injury repair. Calvarial bones are separated by fibrous joints called cranial sutures, whose patency allows postnatal skull expansion to accommodate brain growth<sup>4</sup>. The meninges contain a heterogeneous population of cells, including fibroblasts, SPCs, blood and lymphatic vessels, and immune cells<sup>2</sup>. The meningeal lymphatic system is a network of lymphatic vessels located at the brain border. Unlike other organs, the brain parenchyma is devoid of conventional lymphatic vessels. Instead, interstitial fluid (ISF) reabsorption in brain parenchyma relies on a paravascular (glymphatic) route<sup>5</sup>, in which the space between blood vessels and brain tissues is deployed for cerebrospinal fluid (CSF) influx and ISF efflux. Recent (re)discovery and characterization of meningeal lymphatic vessels has

revealed their functions in brain CSF drainage<sup>6,7</sup>. The meningeal lymphatic outflow of CSF at the brain border is functionally linked with brain glymphatic fluid circulation inside the brain parenchyma<sup>5,8</sup>, which helps remove brain waste and promote neurocognitive function. Studies have shown that the meninges communicate with the skull<sup>9</sup>, as has communication with the brain via meningeal lymphatics<sup>8,10</sup>, while meningeal dura cells actively participate in calvarial bone development and injury repair<sup>10</sup>. However, how the skull functionally integrates with meningeal lymphatics and the brain under pathophysiological conditions remains largely unknown.

Craniosynostosis is a major congenital craniofacial disorder and occurs in 1 in 2000–2500 human births. It is characterized by the premature fusion of cranial suture(s). The suture provides a niche for the SPCs of the calvarial bones, and SPC loss contributes to the premature suture fusion in craniosynostosis<sup>10,11</sup>. In addition to skull dysmorphology, neurocognitive dysfunctions are found in subpopulations of craniosynostosis patients<sup>12,13</sup>. Increased intracranial pressure (ICP) occurs in patients<sup>14,15</sup> and correlates with neurocognitive defects in craniosynostosis<sup>16,17</sup>. Currently, the main treatment for craniosynostosis is complex skull surgery<sup>13,18</sup>, which is invasive and often causes significant blood loss in young patients. In many cases, the calvarial bones fuse again (resynostose) with a chronically high level of ICP, necessitating re-operation<sup>19,20</sup>. We recently established an animal model of neurological deficits in craniosynostosis using *Twist1*<sup>+/-</sup> mice<sup>21</sup>, which recapitulate human Saethre-Chotzen syndrome<sup>22,23</sup>. Using a biodegradable material combined with implanted *Gli1*<sup>+</sup> SPCs, we regenerated a functional cranial suture that reduced neurocognitive behavioral deficits in *Twist1*<sup>+/-</sup> craniosynostosis mice<sup>21</sup>. It is important to determine how *Gli1*<sup>+</sup> SPC-based suture regeneration provides beneficial effects on brains.

In this study, we identified a functional circuit of skull-meningeal lymphatics-brain. We discovered meningeal lymphatic morphology and functional impairments in *Twist1*<sup>+/-</sup> mice with craniosynostosis. Loss of SPCs in mutant mice leads to skull dysmorphology and elevated ICP, as well as reduced meningeal VEGF-C, which collectively disrupt meningeal lymphatic vessels. Transplanting *Gli1*<sup>+</sup> SPCs back restores ICP and meningeal lymphatics, resulting in improved cognitive functions. VEGF-C mediates cell-cell interactions between *Gli1*<sup>+</sup> SPCs and lymphatic endothelial cells (LECs). Treating *Twist1*<sup>+/-</sup> mice with VEGF-C enhances meningeal lymphatic functions and rescues defects in ICP, brain fluid homeostasis, and cognitive behaviors, providing a potential therapeutic strategy to treat craniosynostosis.

## RESULTS

### Impaired meningeal lymphatics and brain perfusion in *Twist1*<sup>+/-</sup> mice with craniosynostosis

Skull dysmorphology, as well as structural and functional brain defects, co-exist in *Twist1*<sup>+/-</sup> craniosynostosis patients and mouse models<sup>11,12,21</sup>. Given the close proximity of meningeal lymphatics to both the skull and the brain, we hypothesized that meningeal lymphatic impairment might connect skull and brain defects in craniosynostosis. To test this hypothesis, we examined the morphology of meningeal lymphatic vasculature in *Twist1*<sup>+/-</sup> mice with craniosynostosis (referred to as MUT). We generated *Twist1*<sup>+/-</sup>;*Prox1*-eGFP

mice, in which *Prox1*-eGFP fluorescently labels *Prox1*<sup>+</sup> lymphatic vessels<sup>24</sup>. Following this, we performed ultimate 3D imaging of solvent-cleared organs (uDISCO) in adult mouse heads<sup>25</sup>, a procedure that left the skull nearly transparent (Figure 1A). Three-dimensional reconstructed imaging with light-sheet microscopy showed a decreased density of *Prox1*<sup>+</sup> meningeal lymphatic vessels in the mutant mice (Figure 1B). Next, we used lymphatic vessel endothelial receptor 1 (LYVE1) coupled with *Prox1*-eGFP mouse genetics to specifically label lymphatic vessels. Whole mount immunostaining of LYVE1 and *Prox1*-eGFP in the meninges confirmed significantly reduced meningeal lymphatic coverage in MUT mice (Figures 1C and 1D). To examine meningeal lymphatic drainage functions in mice, 2 ul of Alexa Fluor 647-conjugated ovalbumin (OVA-647) protein was injected intra-cisterna magna (i.c.m.), which allows it to drain to the deep cervical lymph nodes (dCLNs). We measured the presence of this tracer in mouse dCLNs two hours after injection (Figure 1E) using the clear, unobstructed brain/body imaging cocktails and computational analysis (CUBIC) tissue clearing method. There was a significant decrease in OVA-647 drainage to the dCLNs in MUT mice (Figures 1F and 1G; Video S1). Thus, we combined uDISCO, light sheet imaging, CUBIC, and mouse genetic reporters and identified meningeal lymphatic morphology and drainage function defects in *Twist1*<sup>+/-</sup> craniosynostosis mice.

The CSF enters the brain parenchyma along paravascular spaces in between the penetrating arteries and brain tissues, known as the paravascular (glymphatic) pathway<sup>5</sup>. The disruption of meningeal lymphatic vessel function slows paravascular influx of CSF macromolecules into the brain and reduces efflux of macromolecules from the interstitial fluid (ISF) into the brain parenchyma<sup>8</sup>. To determine the effect of meningeal lymphatic defects on brain fluid homeostasis, we examined CSF influx by performing an OVA-647 conjugate i.c.m. injection on *Twist1*<sup>+/-</sup> mice, followed by serial brain sectioning at 1 hr post-injection. The area fraction of OVA-647 was significantly reduced in MUT compared to WT controls (Figures 1H and 1I), suggesting that the brain influx of CSF macromolecules through paravascular pathways is compromised in mutant mice. The i.c.m. injection of tracers is for monitoring CSF influx, while the intra-parenchymal injection of dye is used to assess ISF efflux of biomolecules out of the brain into circulation<sup>8</sup>. Next, we investigated how the ISF efflux from the brain parenchyma is affected by meningeal lymphatic vessel defects in mutant mice. To this end, we performed stereotaxic injection of amyloid-beta42-HyLite488 (A $\beta$ <sub>42</sub>-488), an Alzheimer's Disease (AD)-relevant peptide, and OVA-647 tracer into the corpus striatum (CPu). 1 hour after injection, we collected the whole brain sample, followed by brain serial section analysis (Figure 1J). Larger amounts of the A $\beta$ <sub>42</sub>-488 as well as OVA-647 remained in the brain parenchyma of the MUT mice compared to controls (Figures 1K and 1L), indicating impaired ISF macromolecule efflux from the brain parenchyma as a consequence of meningeal lymphatic vessel disruption in *Twist1*<sup>+/-</sup> craniosynostosis mice. Together, these results suggest that impaired meningeal lymphatics is coupled with CSF influx and ISF efflux defects in the brains of *Twist1*<sup>+/-</sup> mice with craniosynostosis.

## Meningeal lymphatic impairment is rescued by implanted *Gli1*<sup>+</sup> SPCs in *Twist1*<sup>+/-</sup> mice with craniosynostosis

Loss of *Gli1*<sup>+</sup> SPCs contributes to premature cranial suture fusion and leads to skull dysmorphology, resulting in ICP elevation due to craniocerebral disproportion<sup>21,26</sup>. Increased ICP can disrupt meningeal lymphatic functions<sup>27</sup>. Therefore, we hypothesized that elevated ICP drives meningeal lymphatic defects in *Twist1*<sup>+/-</sup> mice with craniosynostosis. To test this hypothesis, we attempted to reduce elevated ICP using our previously established SPC transplantation method<sup>21</sup>. Specifically, we investigated whether adding *Gli1*<sup>+</sup> SPCs back into *Twist1*<sup>+/-</sup> craniosynostosis mice could rescue meningeal lymphatic defects by reducing ICP. We performed a suturectomy and bilaterally implanted *Gli1*<sup>+</sup> SPCs combined with a biodegradable material into *Twist1*<sup>+/-</sup> craniosynostosis mice (Figure 2A). We used *Gli1-Cre<sup>ERT2</sup>;Rosa26-tdTomato* mice to genetically label implanted *Gli1*<sup>+</sup> SPCs and confirmed their presence in the regenerating sutures (Figure 2B, white arrows), as well as in the dura mater where they migrate from the suture area (Figure 2B, white arrowheads). Furthermore, this suture regeneration surgery released the intracranial hypertension of the MUT mice, as evidenced by significantly reduced ICP in *Twist1*<sup>+/-</sup> mice with regenerated sutures (referred to as REG) compared to the MUT mice (Figures 2C–2E). Together, these results suggest that we can use SPC implantation to reduce elevated ICP in mutant mice.

Next, we examined how SPC implantation-mediated ICP reduction impacts meningeal lymphatic vessel morphology and functions in MUT mice. Whole meningeal staining of LYVE1 showed that the lymphatic vessel coverage was restored in REG mice at 3 months (Figures 2F and 2H) but not at 1 month (Figures S1A and S1B) after SPC implantation. In contrast to bilateral implantation, unilateral SPC transplantation on *Twist1*<sup>+/-</sup> mice with bilateral craniosynostosis failed to rescue meningeal lymphatic morphology (Figures S2A and S2D), drainage functions (Figures S2B and S2E), and CSF influx (Figures S2C and S2F). Therefore, we focused on our analyses at 3 months after bilateral SPC implantation. Increased amounts of OVA-647 CSF tracer were detected in the dCLNs of REG mice compared to those in the MUT mice and resembled the tracer levels in WT mice at 2 hr after i.c.m. injection (Figures 2G and 2I). This suggests that SPC implantation can rescue meningeal drainage defects in *Twist1*<sup>+/-</sup> mice with craniosynostosis. Meanwhile, the amount of OVA-647 perfused into the brain parenchyma by CSF in REG mice was comparable to that in WT controls (Figures 2J and 2L). The reduced ISF efflux defect in MUT mice was also restored by *Gli1*<sup>+</sup> SPC implantation, as evidenced by the significantly decreased amount of A $\beta$ <sub>42-488</sub> and OVA-647 remnants in the brain parenchyma (Figures 2K, 2M, S1C and S1D). Thus, *Gli1*<sup>+</sup> SPC implantation in *Twist1*<sup>+/-</sup> mice reduces ICP and meningeal lymphatic defects.

## *Twist1*<sup>+/-</sup> mice phenocopy meningeal lymphatic vessel defects in vessel ablation mice

To evaluate the severity of meningeal lymphatic defects in *Twist1*<sup>+/-</sup> mice with craniosynostosis, we investigated the extent to which *Twist1*<sup>+/-</sup> mice phenocopy meningeal lymphatic vessel defects in vessel ablation mice. For this, we used a Visudyne-based pharmacological approach, which has been established to selectively ablate the meningeal lymphatic vessels without damaging the surrounding blood vasculature<sup>8,28</sup>. Visudyne was i.c.m. injected into the CSF, followed by non-thermal 689 nm wavelength laser treatment.

Injection of the vehicle followed by photoconversion served as the negative control (Sham). Mice treated by Visudyne i.c.m. injection without photoconversion showed no changes in ICP and neurocognitive behaviors (data not shown). The use of this method effectively ablated meningeal lymphatic vessels (Figures 3A and 3C), resulting in functional defects in the dCLN drainage of CSF macromolecules (Figures 3B and 3D). In terms of meningeal lymphatic vessel coverage and drainage function defects, *Twist1<sup>+/-</sup>* mice displayed a half severity level of that in vessel ablation mice (Figures 3C and 3D). The CSF influx defect in the brain parenchyma of *Twist1<sup>+/-</sup>* mice is about one-fourth the severity of that in vessel ablation mice (Figures 3E and 3G), whereas the ISF efflux defect is around half the severity of that in vessel ablation mice, regardless of A $\beta$ <sub>42-488</sub> or OVA-647 injection (Figures 3F, 3H, S1E and S1F). Together, we showed that *Twist1<sup>+/-</sup>* mice phenocopy meningeal lymphatic defects in vessel ablation mice, including reduced meningeal lymphatic vessel coverage and dCLN drainage, as well as impaired CSF influx and ISF efflux of the brain parenchyma.

### **Meningeal lymphatic vessel ablation blocks SPC implantation-mediated beneficial effects on neurocognitive functions in *Twist1<sup>+/-</sup>* mice with craniosynostosis**

We reasoned that meningeal lymphatic disruption might drive neurocognitive defects in *Twist1<sup>+/-</sup>* craniosynostosis mice. This is because meningeal lymphatic vessel impairment can induce cognitive behavioral abnormalities due to impaired CSF influx and ISF efflux<sup>8</sup>, which occurred in our MUT mice. We have previously established cognitive behavioral abnormalities in *Twist1<sup>+/-</sup>* craniosynostosis mice<sup>21</sup>, recapitulating features of human Saethre-Chotzen syndrome. *Gli1<sup>+</sup>* SPC implantation successfully rescued neurocognitive defects in MUT mice<sup>21</sup>. Here we investigated if and to what extent meningeal lymphatic restoration in *Twist1<sup>+/-</sup>* REG mice is responsible for neurocognitive improvement. To address this issue, we performed Visudyne-based meningeal lymphatic vessel ablation followed by behavioral analysis on *Twist1<sup>+/-</sup>* craniosynostosis mice with *Gli1<sup>+</sup>* SPC implantation (referred to as REG + Vessel ablation), while REG mice with vehicle i.c.m. injection coupled with photoconversion served as the controls (referred to as REG + Sham) (Figure 3I). The reduced ICP in *Twist1<sup>+/-</sup>* mice with regenerated sutures was elevated after lymphatic vessel ablation (Ves- [Vessel ablation], Figures 2C and 2E). The novel object test showed that meningeal lymphatic vessel ablation significantly reduced preference for the novel object in REG mice, resembling that in MUT mice (Figures 3J and 3L). This suggests that hippocampus-dependent spatial recognition improvement by implanted SPCs in REG mice is abolished after meningeal lymphatic vessel ablation. The three-chamber test showed that REG mice exhibited a strong preference for the stranger mouse in the sociability session and the novel stranger mouse in the social memory session, while the REG mice after vessel ablation lost these social behavioral improvements and displayed similar cognitive defects as the MUT mice (Figures 3K, 3M, and 3N). Therefore, meningeal lymphatic vessel ablation blunts the SPC implantation-mediated benefits to cognitive behaviors in REG mice. Together, suture SPC loss causes skull dysmorphology and elevated ICP, which in turn disrupts meningeal lymphatics leading to brain perfusion and neurocognitive defects. All of these defects can be rescued by adding SPCs back to restore ICP and meningeal lymphatics in *Twist1<sup>+/-</sup>* mice with craniosynostosis.

## SPCs promote lymphatic endothelial cell (LEC) growth and migration

We previously reported a loss of *Gli1*<sup>+</sup> SPCs in *Twist1*<sup>+/-</sup> mice with craniosynostosis<sup>26</sup>, which is likely due to *Twist1* deficiency-induced proliferation reduction and premature osteogenic differentiation of *Gli1*<sup>+</sup> SPCs (Figure S3). *Gli1*<sup>+</sup> SPC loss in *Twist1*<sup>+/-</sup> mice is coupled with the diminished meningeal lymphatic vasculature found in this study. So far, we have shown that adding SPCs back can promote meningeal lymphatics by modulating ICP. To further investigate mechanistic links between SPCs and meningeal lymphatic vessels, we explored the potential direct interaction between *Gli1*<sup>+</sup> SPCs and lymphatic endothelial cells (LECs). *Gli1*<sup>+</sup> SPC implantation can regenerate a functional suture and expand the underlying meningeal dura, which contains abundant SPCs<sup>21</sup>. We first generated *Gli1-Cre<sup>ERT2</sup>;Rosa26-tdTomato* mice with *Cre* expression induction by Tamoxifen injection for 48 hours. We found that genetically labeled *Gli1*-tdTomato<sup>+</sup> cells are rarely overlapped with *Col1a1*<sup>+</sup> fibroblasts (Figure S4A, S4B and S4E) as well as NG2<sup>+</sup> and  $\alpha$ SMA<sup>+</sup> cells (Figure S4A, S4C, S4D and S4F) at different dura regions such as the transverse sinus (TS), sagittal sinus (SS), and non-sinus (NS) area. *Gli1*-tdTomato<sup>+</sup> cells are proximally localized with LYVE1<sup>+</sup> meningeal LECs at different dura regions, including the middle meningeal artery (MMA), superior sagittal sinus (SS), and TS (Figure 4A), suggesting that *Gli1*<sup>+</sup> SPCs in the dura might directly interact with meningeal lymphatic vessels. To test this hypothesis, we performed a co-culture of phenotypically characterized human primary LECs (Figure S4G–S4J) with conditional medium (CM) from *Gli1*<sup>+</sup> SPCs or human induced pluripotent stem cell (hiPSC) control cells. The culture media from *Gli1*<sup>+</sup> SPCs or hiPSCs (control) were transferred to the LECs, followed by proliferation and wound healing assays (Figure 4B). EdU incorporation assays showed that there is a significant increase of EdU<sup>+</sup> LECs after the treatment of SPC-CM compared to controls (Figures 4C and 4D). There was an increase in the percentage of Ki67<sup>+</sup> LECs after SPC-CM exposure (Figures 4E and 4F). The phosphohistone H3 (p-H3) staining showed that SPC-CM promotes the mitotic progression of LECs (Figures 4G and 4H). These results indicated that SPC-CM could promote LEC proliferation. Wound healing assays showed that LECs treated with SPC-CM have a faster migration speed than those treated with control-CM (Figures 4I and 4J), suggesting that SPC-CM promotes the LEC migration. These experiments were performed using CM without direct contact between SPCs and LECs. Therefore, SPCs might secrete factors that are important for meningeal LEC functions.

## *Gli1*<sup>+</sup> SPCs secrete VEGF-C that is critical for mediating SPC-LEC interaction

To investigate molecular mechanisms underlying the SPC-LEC interaction, we focused on VEGF-C signaling. VEGF-C signals through VEGFR3 and plays an essential role in meningeal lymphatic vessel development and maintenance<sup>6,29</sup>. We found that VEGF-C is highly expressed in *Gli1*<sup>+</sup> SPCs in both cranial sutures and meningeal dura (Figure 5A). Importantly, VEGF-C-expressing *Gli1*<sup>+</sup> SPCs are localized in the proximity of LYVE1-labeled meningeal LECs (Figure 5A). We performed i.c.m. injection of VEGF-C in *Prox1*-eGFP mice (Figure 5C) and found that VEGF-C promotes meningeal lymphatic vessel cell proliferation *in vivo*, as reflected by a significant increase in EdU<sup>+</sup> and Ki67<sup>+</sup> LECs labeled by LYVE1 and *Prox1*-eGFP in VEGF-C treated mice (Figures 5D, 5E, and 5S). We hypothesized that SPCs secrete VEGF-C that binds to VEGFR3 in LECs to promote their growth and migration. To test this hypothesis, we performed an ELISA and found

that VEGF-C was detected with a drastically increased concentration in the SPC-CM compared to controls (Figure 5B), suggesting that VEGF-C can be secreted by SPCs. To investigate how SPC-CM impacts VEGFR3 downstream signaling, we performed a Western blot (WB) on LECs exposed to SPC-CM or control-CM. The expression of VEGFR3, the main receptor of VEGF-C in lymphatic vessels, was significantly increased in LECs with SPC-CM treatment compared to controls (Figures 5F and 5G). SPC-CM treatment also significantly increased the expression of downstream signaling molecules, including the phosphorylated ERK (p-ERK), Akt (p-AKT), and ribosome protein S6 (p-S6) (Figures 5F and 5G). These results suggest that SPCs secrete VEGF-C, which then activates VEGFR3 signaling in adjacent LECs, leading to their increased proliferation and migration. To investigate the functional importance of VEGF-C in mediating the SPC-LEC crosstalk, an antibody against VEGF-C was added to the SPC-CM and the control medium, while the IgG antibody isotype was used as the negative control. VEGF-C blockage significantly blunted SPC-CM-mediated promotion of LEC proliferation, as evidenced by robustly reduced EdU<sup>+</sup> cells in SPC-CM treatment with VEGF-C antibodies (Figures 5H and 5I). Similarly, the SPC-CM-mediated enhancement of LEC migration was also diminished by VEGF-C blockage based on a wound healing assay (Figures 5J and 5K). Together, these results suggest that SPCs communicate with meningeal LECs through VEGF-C-VEGFR3 signaling, leading to the promotion of LEC cell proliferation and migration.

### **VEGF-C treatment restores meningeal lymphatic morphology and drainage function in *Twist1*<sup>+/-</sup> mice with craniosynostosis**

Our study implicates VEGF-C-VEGFR3 signaling as a potential therapeutic target for treating neurological defects in craniosynostosis. We genetically labeled *Gli1*<sup>+</sup> SPCs and performed meningeal whole mounting staining of VEGF-C and LYVE1. Direct co-labeling of meningeal dura further confirmed that *Gli1*<sup>+</sup> SPCs adjacent to meningeal lymphatic vessels express a high level of VEGF-C, while VEGF-C is mainly localized to *Gli1*<sup>+</sup> cells (Figure 6A). Together, these results suggest that *Gli1*<sup>+</sup> SPCs are a cellular source of VEGF-C in meningeal dura. The loss of *Gli1*<sup>+</sup> SPCs in cranial sutures and dura in *Twist1*<sup>+/-</sup> mice with craniosynostosis is expected to cause VEGF-C downregulation in the meninges. Indeed, our ELISA showed that there is a significant decrease in the concentration of VEGF-C in the meninges of *Twist1*<sup>+/-</sup> mice with craniosynostosis (Figure 6B). We then hypothesized that adding VEGF-C back might reverse the phenotypes of MUT mice. To this end, we used i.c.m. delivery of VEGF-C by adenovirus gene therapy using adeno-associated virus serotype 1 (AAV1), which has been previously used to rejuvenate meningeal lymphatic draining function<sup>8</sup>. We performed an i.c.m. injection to deliver the AAV1-mVEGF-C or the AAV1-GFP control virus into the CSF of MUT and control WT mice, allowing 4 weeks for the virus to spread and fully express VEGF-C in the meninges (Figure 6C). In MUT mice with AAV1-VEGF-C treatment, ICP elevation was reduced to a level comparable to that of the control groups (Figure 6D). Treatment of *Twist1*<sup>+/-</sup> craniosynostosis mice (MUT) with AAV1-VEGF-C significantly promoted meningeal lymphatic vessel growth, which was comparable to that in their WT control counterparts (Figures 6E and 6G). As expected, increased meningeal lymphatic vessel growth by VEGF-C treatment was coupled with its functional improvement, as evidenced by more OVA-647 CSF tracer drainage to the dCLNs in VEGF-C overexpression groups (Figures 6F and 6H).



VEGF-D is homologous to VEGF-C and regulates lymphangiogenesis<sup>30</sup>. To examine effects of VEGF-D on meningeal lymphatics, we generated AAV1-VEGF-D viruses, which were introduced into WT or *Twist1*<sup>+/-</sup> craniosynostosis mice via i.c.m injection. The meningeal lymphatic vessels were partially restored in MUT mice (Figures S6A and S6F). Similar partial rescue effects were also observed in the drainage functions of meningeal lymphatic vessels (Figures S6B and 6G). However, VEGF-D is not as potent as VEGF-C in rescuing meningeal lymphatic morphology and drainage functions. Together, these results suggest that VEGF-C (and VEGF-D to a lesser extent) promotes meningeal lymphatic vessel growth as well as its drainage function in *Twist1*<sup>+/-</sup> mice with craniosynostosis.

### **VEGF-C treatment rescues brain fluid and behavioral deficits in *Twist1*<sup>+/-</sup> mice with craniosynostosis**

To investigate how AAV1-VEGF-C treatment influences brain fluid homeostasis, we examined paravascular CSF macromolecule influx in the brain parenchyma. AAV1-VEGF-C treatment significantly increased brain perfusion by CSF tracer OVA-647 in both control and MUT mice (Figures 6I and 6K), resulting in a full rescue of CSF influx defects in MUT mice. Independent of the nature of fluorescent tracers A $\beta$ <sub>42-488</sub> or OVA-647, levels of remnants were significantly reduced in the brains of MUT mice treated with AAV1-VEGF-C compared to control groups treated with AAV1-eGFP (Figures 6J, 6L, S1G and S1H), suggesting that VEGF-C overexpression rescued ISF efflux defects in MUT mice. In parallel, we examined the effects of VEGF-D on brain fluid homeostasis. VEGF-D treatment had a partial rescue of CSF influx and ISF efflux defects in *Twist1*<sup>+/-</sup> craniosynostosis mice (Figures S6D, S6E, S6I and S6J), although the rescuing effect was not as robust as VEGF-C.

To investigate the beneficial effects of AAV1-VEGF-C treatment on animal behaviors, we raised a cohort of WT and *Twist1*<sup>+/-</sup> craniosynostosis mice (MUT) with AAV1-eGFP or AAV1-VEGF-C i.c.m. injection, followed by behavioral analyses at 1 month post-injection. Three-chamber assays showed that AAV1-VEGF-C treatment significantly rescued sociability and social memory defects in MUT mice, with minimal effects on WT control mice (Figures 7A, 7C and 7D). The novel object test showed that AAV1-VEGF-C treatment fully rescued hippocampus-dependent spatial recognition defects in MUT mice (Figures 7B and 7E). Rotarod assays were used to monitor motor learning behavior (Figure 7F), which was robustly impaired in MUT mice (Figure 7G). AAV1-VEGF-C treatment mitigated and nearly fully rescued this motor learning defect (Figure 7G). In parallel, we examined the effect of VEGF-D treatment on animal behaviors. The three-chamber test showed that VEGF-D treatment failed to significantly increase the sociability and social novelty function of the MUT mice (Figures S6L and S6M). Similarly, the novel object recognition test showed that the hippocampus-dependent spatial recognition in MUT mice was not significantly improved by VEGF-D (Figures S6N and S6O). The rotarod assay showed that the motor learning defect in MUT mice was partially rescued by VEGF-D treatment (Figure 6K). Together, these results suggest that meningeal lymphatic vessel activation by VEGF-C treatment can effectively rescue brain fluid homeostasis defects as well as neurocognitive abnormalities in *Twist1*<sup>+/-</sup> mice with craniosynostosis.

## DISCUSSION

Our studies revealed a functional integration of the skull with meningeal lymphatics and the brain (Figure S7). Meningeal lymphatic vessels are functionally connected with the glymphatic system to regulate fluid homeostasis in the brain parenchyma<sup>5,8</sup>. Studies have separately revealed the meninges communication with the skull and the interaction between the meninges and the brain<sup>8,9</sup>. How skull-meningeal lymphatics-brain functionally integrate beyond their anatomic closeness remains largely unknown and is addressed in this study. We found that SPC-derived VEGF-C, which itself does not restore the skull dysmorphology, can rescue the neurocognitive defects in craniosynostosis through improving the lymphatic functions. Factors crucial in regulating meningeal lymphatics remain largely unknown<sup>31</sup>. We showed that cranial SPCs are a key pathophysiological modulator of meningeal lymphatics. Loss of suture SPCs leads to premature suture fusion, skull dysmorphology, and elevated ICP, which disrupts meningeal lymphatics. Meanwhile, dura SPCs directly interact with meningeal lymphatic endothelial cells (LECs) by secreting VEGF-C, which activates VEGFR3 in LECs to promote their proliferation and migration. Therefore, we identified SPCs as the key cellular source of VEGF-C, which plays crucial roles in meningeal lymphatic development and homeostasis<sup>6,29</sup>.

We found that meningeal lymphatic vasculature plays an essential role in craniosynostosis. Meningeal lymphatic vessel defects have been identified in Alzheimer's and Parkinson's diseases, which are aging-related neurological disorders<sup>31</sup>. Toxic macromolecules and waste products in the CNS parenchyma are removed from the brain by being transported into blood vessels via transvascular clearance<sup>32</sup>. As transvascular clearance gradually deteriorates with age, the increased burden of waste clearance is passed onto the meningeal lymphatic system<sup>32</sup>. Overall, aging is a critical factor in assessing meningeal lymphatics, and it remains unclear how important meningeal lymphatics is in regulating brain tissue homeostasis at developmental stages when blood vessel-based transvascular systems remain relatively intact. Here, we demonstrated that defective meningeal lymphatics can cause neurocognitive defects in craniosynostosis, and their restoration is sufficient to rescue these defects. Our study establishes meningeal lymphatics as a key pathological factor in the developmental disorder craniosynostosis.

Our studies provide insights into the disease mechanisms of craniosynostosis. The *in vitro* studies identified cell-autonomous roles of *Twist1* deficiency in *Gli1*<sup>+</sup> cells. *Twist1* deficiency causes the reduction of *Gli1*<sup>+</sup> cell proliferation and their premature osteogenic differentiation. These results explain the depletion of *Gli1*<sup>+</sup> SPCs leading to synostosis in craniosynostosis. A recent study suggested abnormal meningeal lymphatic networks in craniosynostosis<sup>33</sup>. This finding was carried out using *Twist1<sup>fl/fl</sup>;Sm22a-Cre* homozygous knockout mice, which is different from *Twist1<sup>+/-</sup>* heterozygous mutations in human Saethre-Chotzen syndrome. *Twist1<sup>fl/fl</sup>;Sm22a-Cre* mice have severe phenotypes and show defects in cerebral veins, osteoblast differentiation, and suture and skull morphologies, as well as partial embryonic lethality<sup>14</sup>. In contrast, *Twist1<sup>+/-</sup>* mice have milder phenotypes and show reduced SPC numbers with their premature osteogenic differentiation but are viable and fertile<sup>26</sup>, which more faithfully recapitulates human Saethre-Chotzen syndrome. Using the *Twist1<sup>+/-</sup>* mouse as a genetically and physiologically relevant animal

model of craniosynostosis, we showed meningeal lymphatic morphology and functional defects in drainage, CSF influx, and ISF efflux in the brain leading to neurocognitive dysfunctions. Our studies provided a comprehensive phenotypical characterization of meningeal lymphatics in craniosynostosis. We further demonstrated that meningeal lymphatic dysfunction is a key disease mechanism that drives the neurocognitive defects in craniosynostosis. Our skull-meningeal lymphatics-brain circuit dysregulation explains, at the mechanistic level, the comorbidity of skull dysmorphology and neurocognitive defects in craniosynostosis.

We identified meningeal lymphatics as a potential therapeutic target for treating craniosynostosis. Current clinical treatment for craniosynostosis is a complex and invasive surgery with substantial blood loss and possible resynostosis<sup>13,18</sup>, necessitating re-operation<sup>19,20</sup>. We recently established an SPC-based suture regeneration approach to decrease ICP and mitigate neurological defects in *Twist1*<sup>+/-</sup> craniosynostosis mice<sup>21</sup>. How decreasing ICP by implanted SPCs provides beneficial effects on the brain remains unknown. Here, we demonstrated that meningeal lymphatic restoration is a key mediator of SPCs' beneficial effects. Importantly, VEGF-C treatment without SPC implantation is sufficient to rescue major meningeal lymphatic and neurocognitive defects in *Twist1*<sup>+/-</sup> mice with craniosynostosis. Overall, both SPC implantation and VEGF-C signaling activation can promote meningeal lymphatic function, which in turn enhances neurocognitive functions. Future studies should determine the efficacy and safety of SPC implantation and VEGF-C gene therapy as therapeutic strategies in treating craniosynostosis. In summary, the functional integration of the skull-meningeal lymphatics-brain is orchestrated by SPCs via VEGF-C signaling, which are disrupted in craniosynostosis. SPCs are a key cellular source of VEGF-C and a key cell type in modulating meningeal lymphatic functions. Meningeal lymphatic promotion by SPC implantation or VEGF-C gene therapy might provide a promising therapeutic strategy for treating craniosynostosis.

### Limitations of the study

Our SPC implantation leads to the whole meningeal lymphatic restoration in *Twist1*<sup>+/-</sup> craniosynostosis mice. How a local SPC implantation leads to the global meningeal lymphatic recovery remains to be investigated. In addition to ICP relief and SPC-derived VEGF-C, it will be interesting to determine whether dural fibroblasts or pericytes secrete VEGF-C contributing to the meningeal lymphatic restoration. Another limitation of this study is that we do not know whether different type(s) of fibroblasts have the similar effects as Gli1<sup>+</sup> SPCs in rescuing meningeal lymphatic and cognitive defects in *Twist1*<sup>+/-</sup> craniosynostosis mice. Our studies suggest that ICP relief by SPC implantation in *Twist1*<sup>+/-</sup> mice initially triggers lymphatic vessel restoration, which in turn helps reduce ICP and forms a positive feedback loop along the suture regeneration. However, the exact sequence and causative relationship between ICP relief and lymphatic vessel restoration remain to be experimentally determined.

## STAR★METHODS

### RESOURCE AVAILABILITY

**Lead contact**—Further information and requests for resources and reagents should be directed to and will be fulfilled by the lead contact, Jianfu Chen (jianfu@usc.edu).

**Materials availability**—All new reagents will be made available upon request for scientific research while a completed Materials Transfer Agreement may be required.

**Data and code availability**—All data reported in this paper will be shared by the lead contact upon request.

This paper does not report original code.

Any additional information required to reanalyze the data reported in this paper is available from the lead contact upon request.

### EXPERIMENTAL MODEL AND STUDY PARTICIPANT DETAILS

**Animals**—All animal experiments were conducted in accordance with the guidelines of the Institutional Animal Care and Use Committee (IACUC), University of Southern California. Mice were housed under standard conditions and given chow and water ad libitum. *Twist1*<sup>+/-</sup> mice were obtained from Dr. Robert Maxson (University of Southern California; JAX no.002221). C57BL/6J (JAX no. 000664), *Gli1*-Cre<sup>ERT2</sup> (JAX no. 007913), ROSA26<sup>LoxP-STOP-LoxP-tdTomato</sup> (JAX no. 007905) were purchased from the Jackson Laboratory. *Prox1*-eGFP mice were obtained from Dr. Young-Kwon Hong<sup>24</sup>. Animals were maintained on mixed C57BL/6J and 129S6 backgrounds and included both males and females. The skull progenitor cell implantation surgery was performed on postnatal day 14. Behavioral tests, intra-cisterna magna injection, intracranial injection and the Visudyne-based meningeal lymphatic vessel ablation surgeries were performed at 8–10 weeks old or three months after SPC implantation.

**Cell lines**—The *Gli1*<sup>+</sup> suture progenitor cells were isolated from *Gli1*-Cre<sup>ERT2</sup>;ROSA26<sup>LoxP-STOP-LoxP-tdTomato</sup> P1 mouse cranial sutures as described in previous studies<sup>21</sup>. The minced suture tissues were digested by TrypLE at 37°C. *Gli1*-tdTomato<sup>+</sup> cells were sorted by flow cytometry and cultured in aMEM based complete medium.

The human primary lymphatic endothelial cells were generated and obtained from Hong Lab<sup>35</sup>. culture conditions for different cell lines are detailed in the “methods details” section below.

HEK293T cells were purchased from ATCC and cultured following the manufacturer’s instruction (ATCC, Cat #CRL-3216).

### METHOD DETAILS

**Generation and osteogenic differentiation of *Gli1*<sup>+</sup> suture progenitor cells**—The Cre-dependent tdTomato expression in *Gli1*-Cre<sup>ERT2</sup>;ROSA26<sup>LoxP-STOP-LoxP-tdTomato</sup>

mice was induced by intraperitoneal injection (i.p.) of Tamoxifen (Sigma Aldrich, T5648, 20 mg/ml in corn oil) at a dosage of 1.5 mg/10 g body weight daily at two days before euthanasia. The sagittal and coronal sutures of P1 *Gli1-Cre<sup>ERT2</sup>;ROSA26<sup>LoxP-STOP-LoxP-tdTomato</sup>* pups were excised within 0.5 mm of abutting bones on both sides under a dissection microscope (Leica, M60). The attached periosteum and dura mater were removed and suture tissues were minced and digested by TrypLE (GIBCO, 1897328) at 37°C. The undigested tissues were removed by filtering through a 40 mm cell strainer (Falcon, 352340) and tdTomato<sup>+</sup> cells were sorted by flow cytometry (BD FACS Aria II system). The tdTomato<sup>+</sup> cells were cultured in aMEM (GIBCO, 2065542) supplemented with 10% FBS (GIBCO, 2100184), 2 mM L-glutamine (Contained in antibiotics), 55 mM 2-mercaptoethanol (GIBCO, 2090354), 100 U/ml penicillin, and 100 mg/ml streptomycin (GIBCO, 2019321). Donor *Gli1*<sup>+</sup> SPCs were cultured and passaged once. Then the SPCs were harvested for implantation without further sorting at confluency of ~90%. The osteogenic differentiation was performed using StemPro Osteogenesis Differentiation Kit (Gibco, Cat # A1007201) according to the manufacturer's instructions. Briefly, the isolated *Gli1*<sup>+</sup> cells were seeded into 12-well plates or Millicell EC slides (Millipore, Cat #PEZGS0416) at 5 × 10<sup>3</sup> cells/m<sup>2</sup> and cultured for two days. Then the media was replaced with Complete Osteogenic Differentiation Medium (Gibco, Cat # A1007201). The Sp7 immunofluorescent staining was performed at 48 hours after osteogenic incubation. For Alizarin Red staining, cells were fixed in 4% PFA for 30 min at 14 days after osteogenic differentiation, followed by staining with 2% Alizarin Red solution (pH 4.2) for 2–3 min.

**Human primary lymphatic endothelial cell (LEC) isolation and culture**—The human primary LECs were isolated from deidentified, otherwise-discarded human foreskins as previously described<sup>34</sup> under the approval of the Institutional Review Board (IRB) at the University of Southern California (Principal Investigator: Young-Kwon Hong). Isolated primary cells were characterized and cultured in media based on Endothelial Basal Media (EBM, Lonza, Cat #CC-3124) or modified MCDB131 media (Sigma-Aldrich, Cat #M8537) as previously described<sup>35</sup>. All primary cells were used for the experiments in this study before they reached eight passages.

**Tissue collection and processing**—Animals were deeply anesthetized and transcardially perfused with phosphate-buffered saline (PBS) followed by 4% paraformaldehyde (PFA). After perfusion, the deep cervical lymph nodes and brains were dissected and fixed in 4% PFA for 12 or 24 hours respectively at 4°C. The fixed lymph nodes were washed with PBS, dehydrated with 30% sucrose (pH 7.4 in PBS) and snap frozen in Tissue-Plus O.C.T. compound (Thermo Fisher Scientific, Cat #23-730-571). The fixed brains were washed with PBS and stored in PBS with 0.02 % azide at 4°C for sectioning. The top of the skull (skullcap) was separated from the skull base using surgical scissors and fixed in 4% PFA for 12 hours at 4°C. The fixed skullcap was washed with PBS, decalcified in 10% EDTA (pH 7.4) for three days at room temperature. Then the decalcified skullcap was dehydrated with 30% sucrose (pH 7.4 in PBS) and snap frozen in Tissue-Plus<sup>®</sup> O.C.T. compound. For dura whole-mount staining, after fixation in 4% PFA, the dura was carefully peeled from the skullcap using fine-tip forceps and washed with PBS three times (5 min each time). Then the dura was mounted on a glass slide. The fixed and frozen lymph

nodes and skullcap were sliced using a cryostat (Leica, Cat #CM1950) with thickness of 30  $\mu\text{m}$  and 12  $\mu\text{m}$  respectively. The fixed brains were sliced (150  $\mu\text{m}$  thick coronal section) using a vibratome (Ted Pella, Cat #10111N). Sections were stored in PBS with 0.02 % azide at 4°C for further use.

**uDISCO tissue clearing and 3D imaging**—The uDISCO tissue clearing was performed as described in previous studies with minor modifications<sup>25</sup>. Briefly, the mice were deeply anesthetized with an intraperitoneal injection of Ketamine/Xylazine (100/10 mg/kg). The anesthetized mice were perfused with PBS containing heparin (10 U/ml) followed by 4% PFA. The mouse heads were dissected and post-fixed in 4% PFA overnight at 4°C. The samples were washed with PBS three times over the course of a day at RT and then decalcified in 20% EDTA (Sigma, Cat. E9884) for 5 days with continuous shaking at 37 °C. The decalcified samples were incubated sequentially in 30%, 50%, 70%, 80%, 90%, 96%, and 100% tert-butanol (Sigma, Cat. 360538) at 37 °C for 12 hours each for dehydration. In the clearing step, the samples were sequentially incubated in BABB [benzyl alcohol (Sigma, Cat. 402834) + benzyl benzoate (Sigma, Cat. B6630) 1:2] for 3–6 hours and diphenyl ether (DPE) (Sigma, Cat. 240834) at a ratio of 15:1 BABB to DPE (BABB-D) for 3–6 hours at room temperature (RT). 3D Images datasets were captured by LaVision Light Sheet microscope (California Institute of Technology, Biological Imaging Facility). The datasets were analyzed for 3D visualization using Imaris 9 imaging analysis software (Bitplane).

**Intracranial pressure measurement**—Intracranial pressure was measured as described previously with minor modifications<sup>21</sup>. Briefly, mice were anaesthetized with 2% isoflurane and their head was fixed on a stereotaxic frame (David KOPF Instruments, Model 900LS). A hole was drilled on the parietal bone that was 2 mm lateral and 2 mm posterior from Bregma. A 10 mL pipette tip (cut to 5 mm in length) used as the sensor guide was inserted into the hole and fixed with dental cement. After the dental cement dried, the sensor guide was filled with sterile PBS and the fiber-optic intracranial pressure probe (FISO Technologies) was inserted until the tip of the probe touched the dura. Caulking material was applied around the probe and the head of the sensor guide to form an airtight seal. Intracranial pressure was recorded with Evolution software (FISO Technologies).

**Stereotaxic surgeries**—Mice were anesthetized with 2% isoflurane frame and aligned on a stereotaxic frame. The skull was exposed and a small craniotomy was made with a thin drill. 1  $\mu\text{l}$  of Alexa Fluor 647-conjugated OVA (0.5  $\mu\text{g}/\mu\text{l}$ , Thermo Fisher Scientific) or 1  $\mu\text{l}$  Alexa Fluor 488-conjugated amyloid- $\beta_{42}$  (0.05  $\mu\text{g}/\mu\text{l}$ ) was injected into striatum (AP +1.4 mm, ML -1.4 mm, DV -3.0 mm) at a rate of 100 nl/min using a 10  $\mu\text{l}$  Hamilton syringe (Hamilton Company, Cat. No. 1701). The syringe needle was left in place for additional 10 min to prevent backflow. Mice were euthanized 60 min after injection for examination.

**AAV1-VEGF-D vector production**—The plasmids pAAV: psubCMV-mVEGF-D-WPRE (gift from Kari Alitalo lab, Addgene plasmid #119226), pAAV2/1 (gift from James M. Willson Lab, Addgene plasmid #112862), and pAdDeltaF6 (gift from James M. Willson Lab, Addgene plasmid #112867) were transfected together into HEK293 T cells (ATCC,

Cat #CRL-3216) with Polyethylenimine (Polyscience, Cat #23966-1). The culture medium was collected after 72 hours of transfection followed by the final collection of both cells and media after 120 hours. The virus particles were precipitated from the medium with 40% polyethylene in 500 mM NaCl and mixed with cell pellets and then the cell pellets were suspended in the solution containing 500 mM NaCl, 40 mM Tris, 2.5 mM MgCl<sub>2</sub> and 25 U/μl of salt-activated nuclease (ArcticZymes, Cat #10977-023). AAVs were extracted from cell lysates using iodixanol step gradients (60% (wt/vol) iodixanol; Cosmo Bio USA, Cat #AXS-1114542-5) and ultracentrifugation at speed of 350000g at 18°C. AAVs were then filtered by Syringe filter units (0.22 μm; Millipore; Cat #SLGP033RS) and concentrated through Amicon filters (100 kDa; Millipore, Cat #UCF910024). The viral titer ( $2.1 \times 10^{13}$  GC/mL) was determined by qPCR analysis of WPRE element.

**Intra-cisterna magna injection**—Mice were anaesthetized with 2% isoflurane and their head was fixed on a stereotaxic frame (David KOPF Instruments, Model 900LS). The head was slightly tilted so that it formed an angle of 120° to the body. A midline incision was made in the skin overlying the neck, and the neck muscles were separated carefully to expose the cisterna magna. 2 μl of Alexa Fluor 647-conjugated OVA (0.5 μg/μl), 2 μl AAV1-CMV-eGFP ( $1.1 \times 10^{13}$  GC/mL, Vector Biolabs), AAV1-CMV-mVEGF-C ( $5.6 \times 10^{13}$  GC/mL, Vector Biolabs), AAV1-CMV-mVEGF-D ( $2.1 \times 10^{13}$  GC/mL) or 2 μl recombinant human VEGF-C (Cys156Ser) protein (2 μg/μl in aCSF, R&D systems, Cat #752-VC-025/CF) was injected into cisterna magna compartment at a rate of 500 nl/min using a 10 μl Hamilton syringe (Hamilton Company, Cat. No. 1701). Before viral injection, the titer of AAV1-CMV-mVEGF-C and AAV1-CMV-mVEGF-D was adjusted to that of AAV1-CMV-eGFP ( $1.1 \times 10^{13}$  GC/mL) by diluting 2 μl aliquot with 8 μl and 1.8 μl artificial CSF (Tocris Bioscience, Cat. #3525) respectively as to have the consistent amount of AAV1-VEGF-C, AAV1-mVEGF-D and AAV1-GFP viral injection. The syringe needle was left in place for additional 3 min to prevent backflow and then was carefully withdrawn. The incision was sutured and the mouse was subcutaneously injected with buprenorphine (0.05 mg/kg) and allowed to recover on heating pad.

**Immunofluorescence**—The cultured *Gli1*<sup>+</sup> cells were fixed with 4% PFA for 15 min at room temperature and washed in PBS three times (5 min each time). The following steps were generally applied for the fixed cultured cells, sections of skullcap with dura or the dura whole mounts. Sample was washed in PBS three times (5 min each time) and then incubated with blocking solution (5% normal goat serum, 1% BSA, 0.3% Triton X-100 in PBS) for 2 h at room temperature. The blocking step was followed by incubation with the following primary antibodies: rat anti-LYVE1 (1:200, Invitrogen, 14-0443-82), rabbit anti-VEGF-C (1:200, NovusBio, NB110-61022), rabbit anti-Ki67 (1:200, Abcam, Cat #ab15580), goat anti-LYVE1 (1:400, R&D systems, Cat #AF2089), rabbit anti-Sp7 (1:400, Abcam, Cat #ab209484), rabbit anti-aSMA (1:200, Abcam, Cat #ab5694), rabbit anti-NG2 (1:200, Sigma-Aldrich, Cat #AB5320), goat anti-PROX1 (1:400, R&D systems, Cat #AF2737), goat anti-VEGFR3 (1:400, R&D systems, Cat #AF743) in blocking solution overnight at 4°C. The rat IgG (1:200, Invitrogen, Cat #31933) and rabbit IgG (1:200, Proteintech, Cat #30000-0-AP) were used as negative control. After washing in PBS three times (5 min each time), the samples were incubated with species-specific fluorescently conjugated

secondary antibodies (1:200, Invitrogen) and DAPI (1:1,000) in blocking solution for 2 h at room temperature. After washing in PBS three times (5 min each time), sections were mounted with Vectashield mounting medium (Vector Laboratories, Cat #H-1000). Images were acquired using Keyence Fluorescence microscope (Keyence, Cat #BZ-X810).

#### ***Twist1* knockdown in suture progenitor cells (SPCs) using shRNA lentivirus**

—*Twist1* knockdown in SPCs was performed using *TWIST1* shRNA lentivirus particles according to manufacturer's protocol (Santa Cruz Biotechnology, Cat #sc-38604-V). Briefly, *Gli1*<sup>+</sup> SPCs were seeded into 24-well plate one day before viral infection. At 60% confluence, the cells were transduced with either 0.6  $\mu$ l of *TWIST1* shRNA lentiviral particles (Santa Cruz Biotechnology, cat #sc-38604-V) or control shRNA lentiviral particles-A (Santa Cruz Biotechnology, cat #sc-108080) per well in the  $\alpha$ -MEM culture medium with 5  $\mu$ g/mL polybrene for 12 hours. Then the media was replaced with  $\alpha$ -MEM culture medium without polybrene.

**EdU incorporation and wound healing assay**—EdU (Thermo Fisher Scientific, Cat #A10044) was dissolved in PBS to 10 mg/ml. *Prox1*-eGFP mice were injected intraperitoneally with EdU (50  $\mu$ g/g body weight) for 8 h before being euthanized. The dura was dissected and fixed as described above. For in vitro experiment, EdU was added into cell culture medium (10  $\mu$ M) at two hours before staining. The *Gli1*<sup>+</sup> cells were fixed as described above and EdU staining was performed according to the manufacturer's instructions using Click-iT plus EdU cell proliferation kit (Thermo Fisher Scientific, Cat #C10637). For the wound healing assay, the conditioned medium was prepared by incubation of *Gli1*<sup>+</sup> SPCs with DMEM (10% FBS) for 48 hours, and the control medium was collected by incubation of hIPSCs after 48 hours. The human LECs were cultured in a 35 mm cell culture dish and the wound healing assays were performed when cells reached 100% confluency. Scratches were made with a 200  $\mu$ l sterile plastic pipette tip on the monolayer cells and then the culture medium was replaced with SPC-CM or control medium. Cells were fixed with 4% paraformaldehyde at 0, 4, 8, 16 and 24 hours after scratching. After washing with PBS for 15 min three times, cells were stained with 0.01% violet acetate (Sigma, Cat #C5042) for 10 min to improve the visibility of cells before imaging.

**In situ hybridization**—Staining was performed using RNAscope Multiplex Fluorescent v2 kit (Advanced Cell Diagnostics, 323100) according to the manufacturer's instructions. Briefly, the fixed dura or cultured *Gli1*<sup>+</sup> cells were treated with H<sub>2</sub>O<sub>2</sub> at room temperature for 10 min followed by protease treatment for 7 min at 40 °C. Probe for *Col1a1* (Advanced Cell Diagnostics, Cat #319371) or *Twist1* (Advanced Cell Diagnostics, Cat #1266861) was then hybridized for 2 h at 40 °C. Signals were amplified using serial amplification reagents provided in the kit and detected by TSA Plus Cyanine 5 system (PerkinElmer, Cat #NEL745001KT).

**Behavioral assays**—Mice were acclimated to the behavior room at least 60 minutes before the behavioral tests. Experimenters were blinded to animal genotypes during behavioral tests and data analyses. The novel object test was performed to measure



hippocampus-dependent spatial recognition. Briefly, the subject mice were habituated to the test chamber ( $L \times W \times H = 48 \text{ cm} \times 27 \text{ cm} \times 22 \text{ cm}$ ) for 10 min. After 24 hours, two identical objects were taped to floor, 10 cm away from the south and north walls. The mouse was placed in the center of the cage facing the east or west wall and allowed to explore for 10 min. After another 24 hours, one of the two objects was replaced with a novel object with a different shape but similar size. The mouse was placed in the test chamber and allowed to explore for 10 min. Mouse behavior was video-recorded and the time exploring the novel or familiar objects was manually documented. The preference index was calculated as  $(T_n - T_f)/(T_n + T_f) \times 100\%$  ( $T_n$  and  $T_f$  represent the time spent exploring the novel and familiar object respectively). The test chamber and objects were thoroughly cleaned with 75% ethanol to remove olfactory cues between each trial.

The three-chamber test was used to measure sociability and social memory. The three-chamber social interaction test was performed in a Plexiglas box ( $L \times W \times H = 60 \text{ cm} \times 42 \text{ cm} \times 22 \text{ cm}$ ) containing three compartments connected by small openings that allowed mice free access to each compartment. Subject mouse was allowed to freely explore the three empty chambers for 10 min. Then a stranger mouse was placed in the inverted wire cup in one side chamber, and an empty wire cup was placed in the other side chamber, and the subject mouse was allowed to freely explore the chambers for 10 min. In the last session, a second stranger mouse was placed in the previous empty wire cup and the subject mouse was allowed to freely explore for another 10 min. The time of the subject mouse spent sniffing each wire cup was quantified and the preference index was calculated as  $(T_{s1} - T_e)/(T_{s1} + T_e) \times 100\%$  or  $(T_{s2} - T_{s1})/(T_{s2} + T_{s1}) \times 100\%$  ( $T_e$ ,  $T_{s1}$ , and  $T_{s2}$  represent the time spent exploring empty, stranger 1, and stranger 2 wire cups respectively). The three-chamber apparatus and wire cups were thoroughly cleaned with 75% ethanol to remove olfactory cues between tests for each mouse.

The rotarod test was used to measure motor learning. This test consists of training and test phases. Mice were first trained by placing them on a rotating rod (Panlab, Havard Apparatus) at a constant speed of 4 rpm until they were able to stay on the rotating rod for 20 seconds. The test phase was performed 24 hours after the training phase. The rotarod apparatus was set to accelerate from 4 to 40 rpm in 300 seconds, and subject mice were placed on the rod initially rotating at 4 rpm. The latency (time) to falling off the rod was determined as the latency to fall (second). Each mouse was tested three times a day at 15 min intervals for five consecutive days.

**Gel synthesis and suture regeneration surgery**—Methacrylated gelatin (GelMA) was synthesized as previously described<sup>21</sup>. Briefly, methacrylic anhydride (MA, Sigma-Aldrich, Cat #276685) was added to 10% gelatin (Sigma-Aldrich, Cat #69391) in PBS (w/v) solution (pH 9.0) at a rate of 0.4~0.5 ml/min with constantly stirring, to achieve a final MA-to-gelatin ratio of 0.3 ml/g. After incubation at 50°C for 2.5~3 h, the solution was dialyzed against distilled water at 40°C for 7 days to remove the excessive methacrylic acid and anhydride, then filtered through a 0.22 mm membrane and freeze-dried. The GelMA was dissolved in aMEM containing 0.5% (w/v) lithium phenyl-2, 4, 6-trimethylbenzoylphosphinate (LAP, TOCRIS, Cat #6146) to achieve the final concentration of 5% (w/v). The modified GelMA (M-GM) was made by mixing 5% GelMA solution with

Matrigel (Corning, 8015323) and 3 mg/mL collagen I (GIBCO, Cat #A10483–01) at 4°C with a volume ratio of 10:2:1.

**Calvarial defect generation**—Two-three weeks old *Twist1*<sup>+/-</sup> mice were confirmed with bilateral coronal suture fusion by microCT scanning and used for suture regeneration surgery. A midline sagittal incision was made in the skin overlying the skull and the skull cap was exposed. The overlying periosteum on the coronal suture area was carefully removed using fine forceps. Then, a drill (NSKI, Cat #Strong90) with round dental burr (Brasseler, Cat #H52. 11. 003) was used to create a rectangular defect with 0.3–0.4 mm width by referencing the residual hallmark of the fused suture and the landmark of a normal coronal suture, while taking care to avoid damage to the sagittal suture and the dura mater underneath. The tdTomato<sup>+</sup> cells isolated from *Gli1*-CreERT2;ROSA26LoxP-STOP-LoxP-eGFP-DTA mice were mixed with modified GelMA (M-GM) at a density of  $5 \times 10^7$  cells/ml and ~2 µl of the cell suspension was added to fill the bone defect. The M-GM was then cured with UV light with a wavelength of 365 nm for a few seconds to completely crosslink the hydrogels. The scalp was then closed with 5–0 nylon sutures.

**Meningeal lymphatic vessel ablation**—The Visudyne-based meningeal lymphatic vessel ablation was performed as previously described<sup>8</sup>. Briefly, mice were anaesthetized with 2% isoflurane and their head was fixed on a stereotaxic frame. 5 µl Visudyne (2 mg/ml, APExBIO, Cat #A8327) was injected into the cisterna magna compartment at a rate of 1 µl/min using a 10 µl Hamilton syringe (Hamilton Company, Cat #1701). The syringe needle was left in place for an additional 3 min to prevent backflow and then was carefully withdrawn. After 15 min, the Visudyne was photoconverted by non-thermal 689 nm wavelength laser light (Coherent Opal Photoactivator, Lumenis) at five different spots (the injection site, the bilateral transverse sinuses, the junction of all sinuses and the superior sagittal sinus) above the intact skull. Each spot was irradiated with a dose of 50 J/cm<sup>2</sup> at an intensity of 600 mW/cm<sup>2</sup> for a total of 83 seconds. Vehicle was injected into the cisterna magna with identical photoconversion treatment as control group.

**Western blot analysis**—The human LECs were lysed RIPA buffer (Cell Signaling, Cat #9806) with protease inhibitor (Thermo Fisher Scientific, Cat #1861278) and PMSF (Thermo Fisher Scientific, Cat #36978) for 30 min at 4 °C. The soluble fraction was isolated with centrifugation at  $14,000 \times g$  at 4 °C for 15 min. The protein concentrations were calculated using the BCA protein assay kit (Thermo Fisher Scientific, Cat #23227) according to the manufacturer's protocol. The protein extracts were loaded and separated by 10% SDS-PAGE and transferred to PVDF membranes (Millipore, Cat #ISEQ00005). Membranes were then blocked with 5% non-fat dry milk dissolved in TBST for one hour at room temperature, then incubated with primary antibodies: anti-VEGFR3 (ReliaTech, Cat #101-M36, 1:1000), anti-pERK (Cell Signaling technology Cat #4370, 1:1000), anti-ERK (Cell Signaling technology, Cat #4695, 1:1000), anti-pAkt (Ser473) (Cell Signaling technology, Cat #4060, 1:1000), anti-Akt (Cell Signaling technology, Cat #9272, 1:1000), anti-pS6 (S240/244) (Cell Signaling technology, Cat #35708, 1:1000), anti-S6 (Cell Signaling technology, Cat #2217, 1:1000), and anti-GAPDH (Cell Signaling technology, Cat #2118, 1:1000) overnight at 4°C, followed by corresponding horseradish-peroxidase

(HRP)-conjugated secondary antibodies (Goat Anti-Rabbit-HRP Conjugate (Biorad, Cat #1705046, 1:2000) and Goat Anti-Mouse-HRP Conjugate (Biorad, Cat #1705047, 1:2000). The protein expression was detected by Azure 300 (Azure Biosystems) and the protein band intensities were analyzed in ImageJ.

## QUANTIFICATION AND STATISTICAL ANALYSIS

All statistical analysis was performed with GraphPad Prism 8 and statistical data are presented as individual points and mean  $\pm$  SEM. The number of mice and the statistical tests used for individual experiments are included in the figure legends. The following symbols are used in the figure legends for P values: ns: not significant; \*:  $P < 0.05$ ; \*\*:  $P < 0.01$ ; \*\*\*:  $P < 0.001$ ; \*\*\*\*:  $P < 0.0001$ .

Both non-parametric tests and parametric tests were used, depending on data normality, for comparing two independent groups (Student's t test) or multiple groups (one-way ANOVA with Tukey post hoc tests). Mice were randomly allocated into experimental groups when possible. Experiments were replicated in multiple animals ( $N \geq 3$  for histological and  $N \geq 10$  for behavior experiments). Behavioral tests were performed by experimenters who were blinded to genotype. Both data from behavioral tests and histological imaging were analyzed by investigators who were blinded to genotype whenever possible.

## Supplementary Material

Refer to Web version on PubMed Central for supplementary material.

## ACKNOWLEDGMENTS

We thank Chen laboratory colleagues for stimulating discussions. We are grateful for Kimi Nakaki's critical reading of the manuscript. This study was supported by grants R01DE030901 (J.C.; Y.C.), R21AG075665 (J.C.), and R21AG070681 (J.C.) from the National Institute of Health. Dr. Li Ma is a post-doctoral fellowship recipient of California Institute for Regenerative Medicine (CIRM) training grant.

## INCLUSION AND DIVERSITY

We support inclusive, diverse, and equitable conduct of research. One or more of the authors of this paper self-identifies as a member of the LGBTQIA+ community.

## REFERENCES

1. Dasgupta K, and Jeong J (2019). Developmental biology of the meninges. *Genesis* 57, e23288. 10.1002/dvg.23288. [PubMed: 30801905]
2. Derk J, Jones HE, Como C, Pawlikowski B, and Siegenthaler JA (2021). Living on the Edge of the CNS: Meninges Cell Diversity in Health and Disease. *Front. Cell. Neurosci* 15, 703944. 10.3389/fncel.2021.703944. [PubMed: 34276313]
3. Nabeshima S, Reese TS, Landis DMD, and Brightman MW (1975). Junctions in the meninges and marginal glia. *J. Comp. Neurol* 164, 127–169. 10.1002/cne.901640202. [PubMed: 810497]
4. Morriss-Kay GM, and Wilkie AOM (2005). Growth of the normal skull vault and its alteration in craniosynostosis: insights from human genetics and experimental studies. *J Anat* 207, 637–653. 10.1111/j.1469-7580.2005.00475.x. [PubMed: 16313397]
5. Iliff JJ, Wang M, Liao Y, Plogg BA, Peng W, Gundersen GA, Benveniste H, Vates GE, Deane R, Goldman SA, et al. (2012). A Paravascular Pathway Facilitates CSF Flow Through the Brain

- Parenchyma and the Clearance of Interstitial Solutes, Including Amyloid  $\beta$ . *Sci Transl Med* 4, 147ra111. 10.1126/scitranslmed.3003748.
6. Aspelund A, Antila S, Proulx ST, Karlsen TV, Karaman S, Detmar M, Wiig H, and Alitalo K (2015). A dural lymphatic vascular system that drains brain interstitial fluid and macromolecules. *J Exp Med* 212, 991–999. 10.1084/jem.20142290. [PubMed: 26077718]
  7. Louveau A, Smirnov I, Keyes TJ, Eccles JD, Rouhani SJ, Peske JD, Derecki NC, Castle D, Mandell JW, Lee KS, et al. (2015). Structural and functional features of central nervous system lymphatic vessels. *Nature* 523, 337–341. 10.1038/nature14432. [PubMed: 26030524]
  8. Mesquita SD, Louveau A, Vaccari A, Smirnov I, Cornelison RC, Kingsmore KM, Contarino C, Onengut-Gumuscu S, Farber E, Raper D, et al. (2018). Functional aspects of meningeal lymphatics in ageing and Alzheimer’s disease. *Nature* 560, 185–191. 10.1038/s41586-018-0368-8. [PubMed: 30046111]
  9. Herisson F, Frodermann V, Courties G, Rohde D, Sun Y, Vandoorne K, Wojtkiewicz GR, Masson GS, Vinegoni C, Kim J, et al. (2018). Direct vascular channels connect skull bone marrow and the brain surface enabling myeloid cell migration. *Nat. Neurosci* 21, 1209–1217. 10.1038/s41593-018-0213-2. [PubMed: 30150661]
  10. Ishii M, Sun J, Ting M-C, and Maxson RE (2015). Chapter Six The Development of the Calvarial Bones and Sutures and the Pathophysiology of Craniosynostosis. *Curr Top Dev Biol* 115, 131–156. 10.1016/bs.ctdb.2015.07.004. [PubMed: 26589924]
  11. Stanton E, Urata M, Chen J-F, and Chai Y (2022). The clinical manifestations, molecular mechanisms and treatment of craniosynostosis. *Dis Model Mech* 15, dmm049390. 10.1242/dmm.049390. [PubMed: 35451466]
  12. Speltz ML, Collett BR, Wallace ER, Starr JR, Craddock MM, Buono L, Cunningham M, and Kapp-Simon K (2015). Intellectual and Academic Functioning of School-Age Children With Single-Suture Craniosynostosis. *Pediatrics* 135, e615–e623. 10.1542/peds.2014-1634. [PubMed: 25713274]
  13. Brooks ED, Beckett JS, Yang J, Timberlake AT, Sun AH, Chuang C, and Persing JA (2018). The Etiology of Neuronal Development in Craniosynostosis. *J Craniofac Surg* 29, 49–55. 10.1097/scs.0000000000004040. [PubMed: 29049144]
  14. Tischfield MA, Robson CD, Gilette NM, Chim SM, Sofela FA, DeLisle MM, Gelber A, Barry BJ, MacKinnon S, Dagi LR, et al. (2017). Cerebral Vein Malformations Result from Loss of Twist1 Expression and BMP Signaling from Skull Progenitor Cells and Dura. *Dev Cell* 42, 445–461.e5. 10.1016/j.devcel.2017.07.027. [PubMed: 28844842]
  15. Hayward R (2005). Venous hypertension and craniosynostosis. *Child’s Nerv Syst* 21, 880–888. 10.1007/s00381-004-1114-0. [PubMed: 15834728]
  16. Renier D, Sainte-Rose C, Marchac D, and Hirsch J-F (1982). Intracranial pressure in craniostenosis. *J Neurosurg* 57, 370–377. 10.3171/jns.1982.57.3.0370. [PubMed: 7097333]
  17. Tamburrini G, Caldarelli M, Massimi L, Santini P, and Rocco CD (2005). Intracranial pressure monitoring in children with single suture and complex craniosynostosis: a review. *Child’s Nerv Syst* 21, 913–921. 10.1007/s00381-004-1117-x. [PubMed: 15871027]
  18. Wolfswinkel EM, Howell LK, Fahradyan A, Azadgoli B, McComb JG, and Urata MM (2017). Is Postoperative Intensive Care Unit Care Necessary following Cranial Vault Remodeling for Sagittal Synostosis? *Plast Reconstr Surg* 140, 1235–1239. 10.1097/prs.0000000000003848. [PubMed: 29176416]
  19. Woods RH, Ul-Haq E, Wilkie AOM, Jayamohan J, Richards PG, Johnson D, Lester T, and Wall SA (2009). Reoperation for Intracranial Hypertension in TWIST1-Confirmed Saethre-Chotzen Syndrome; A 15-Year Review. *Plast Reconstr Surg* 123, 1801–1810. 10.1097/prs.0b013e3181a3f391. [PubMed: 19483581]
  20. Ottelander BKD, Veelen MCV, Goederen RD, Beeten SDVD, Dremmen MH, Loudon SE, Versnel SL, Ouweland AMVD, Dooren MFV, Joosten KF, et al. (2021). Saethre–Chotzen syndrome: long-term outcome of a syndrome-specific management protocol. *Dev Medicine Child Neurology* 63, 104–110. 10.1111/dmcn.14670.

21. Yu M, Ma L, Yuan Y, Ye X, Montagne A, He J, Ho T-V, Wu Y, Zhao Z, Maria NS, et al. (2021). Cranial Suture Regeneration Mitigates Skull and Neurocognitive Defects in Craniosynostosis. *Cell* 184, 243–256.e18. 10.1016/j.cell.2020.11.037. [PubMed: 33417861]
22. Grova M, Lo DD, Montoro D, Hyun JS, Chung MT, Wan DC, and Longaker MT (2012). Models of Cranial Suture Biology. *J Craniofac Surg* 23, S12–S16. 10.1097/scs.0b013e318258ba53.
23. Howard TD, Paznekas WA, Green ED, Chiang LC, Ma N, Luna RIOD, Delgado CG, Gonzalez-Ramos M, Kline AD, and Jabs EW (1997). Mutations in TWIST, a basic helix–loop–helix transcription factor, in Saethre-Chotzen syndrome. *Nat Genet* 15, 36–41. 10.1038/ng0197-36. [PubMed: 8988166]
24. Choi I, Chung HK, Ramu S, Lee HN, Kim KE, Lee S, Yoo J, Choi D, Lee YS, Aguilar B, et al. (2011). Visualization of lymphatic vessels by Prox1-promoter directed GFP reporter in a bacterial artificial chromosome-based transgenic mouse. *Blood* 117, 362–365. 10.1182/blood-2010-07-298562. [PubMed: 20962325]
25. Pan C, Cai R, Quacquarelli FP, Ghasemigharagoz A, Lourbopoulos A, Matryba P, Plesnila N, Dichgans M, Hellal F, and Ertürk A (2016). Shrinkage-mediated imaging of entire organs and organisms using uDISCO. *Nat Methods* 13, 859–867. 10.1038/nmeth.3964. [PubMed: 27548807]
26. Zhao H, Feng J, Ho T-V, Grimes W, Urata M, and Chai Y (2015). The suture provides a niche for mesenchymal stem cells of craniofacial bones. *Nat Cell Biol* 17, 386–396. 10.1038/ncb3139. [PubMed: 25799059]
27. Bolte AC, Dutta AB, Hurt ME, Smirnov I, Kovacs MA, McKee CA, Ennerfelt HE, Shapiro D, Nguyen BH, Frost EL, et al. (2020). Meningeal lymphatic dysfunction exacerbates traumatic brain injury pathogenesis. *Nat Commun* 11, 4524. 10.1038/s41467-020-18113-4. [PubMed: 32913280]
28. Tammela T, Saaristo A, Holopainen T, Ylä-Herttua S, Andersson LC, Virolainen S, Immonen I, and Alitalo K (2011). Photodynamic Ablation of Lymphatic Vessels and Intralymphatic Cancer Cells Prevents Metastasis. *Sci Transl Med* 3, 69ra11. 10.1126/scitranslmed.3001699.
29. Antila S, Karaman S, Nurmi H, Airavaara M, Voutilainen MH, Mathivet T, Chilov D, Li Z, Koppinen T, Park J-H, et al. (2017). Development and plasticity of meningeal lymphatic vessels. *J Exp Med* 214, 3645–3667. 10.1084/jem.20170391. [PubMed: 29141865]
30. Stacker SA, Caesar C, Baldwin ME, Thornton GE, Williams RA, Prevo R, Jackson DG, Nishikawa S, Kubo H, and Achen MG (2001). VEGF-D promotes the metastatic spread of tumor cells via the lymphatics. *Nat. Med* 7, 186–191. 10.1038/84635. [PubMed: 11175849]
31. Mesquita SD, Fu Z, and Kipnis J (2018). The Meningeal Lymphatic System: A New Player in Neurophysiology. *Neuron* 100, 375–388. 10.1016/j.neuron.2018.09.022. [PubMed: 30359603]
32. Sweeney MD, Sagare AP, and Zlokovic BV (2018). Blood–brain barrier breakdown in Alzheimer disease and other neurodegenerative disorders. *Nat. Rev. Neurol* 14, 133–150. 10.1038/nrneurol.2017.188. [PubMed: 29377008]
33. Ang PS, Matrongolo MJ, and Tischfield MA The growth and expansion of meningeal lymphatic networks are affected in craniosynostosis. *Development* 149. 10.1242/dev.200065.
34. Hirakawa S, Hong Y-K, Harvey N, Schacht V, Matsuda K, Libermann T, and Detmar M (2003). Identification of Vascular Lineage-Specific Genes by Transcriptional Profiling of Isolated Blood Vascular and Lymphatic Endothelial Cells. *Am. J. Pathol* 162, 575–586. 10.1016/s0002-9440(10)63851-5. [PubMed: 12547715]
35. Choi D, Park E, Jung E, Cha B, Lee S, Yu J, Kim PM, Lee S, Hong YJ, Koh CJ, et al. (2019). Piezo1 incorporates mechanical force signals to genetic program that governs lymphatic valve development and maintenance. *JCI Insight* 4. 10.1172/jci.insight.125068.

### Highlights

- Meningeal lymphatic dysfunction drives neurocognitive defects in craniosynostosis
- Gli1<sup>+</sup> cell implantation reduces intracranial pressure (ICP) and restores lymphatics
- Gli1<sup>+</sup> cells secrete VEGF-C to promote lymphatic endothelial cell growth
- VEGF-C rescues ICP, brain perfusion, and neurocognitive defects in craniosynostosis

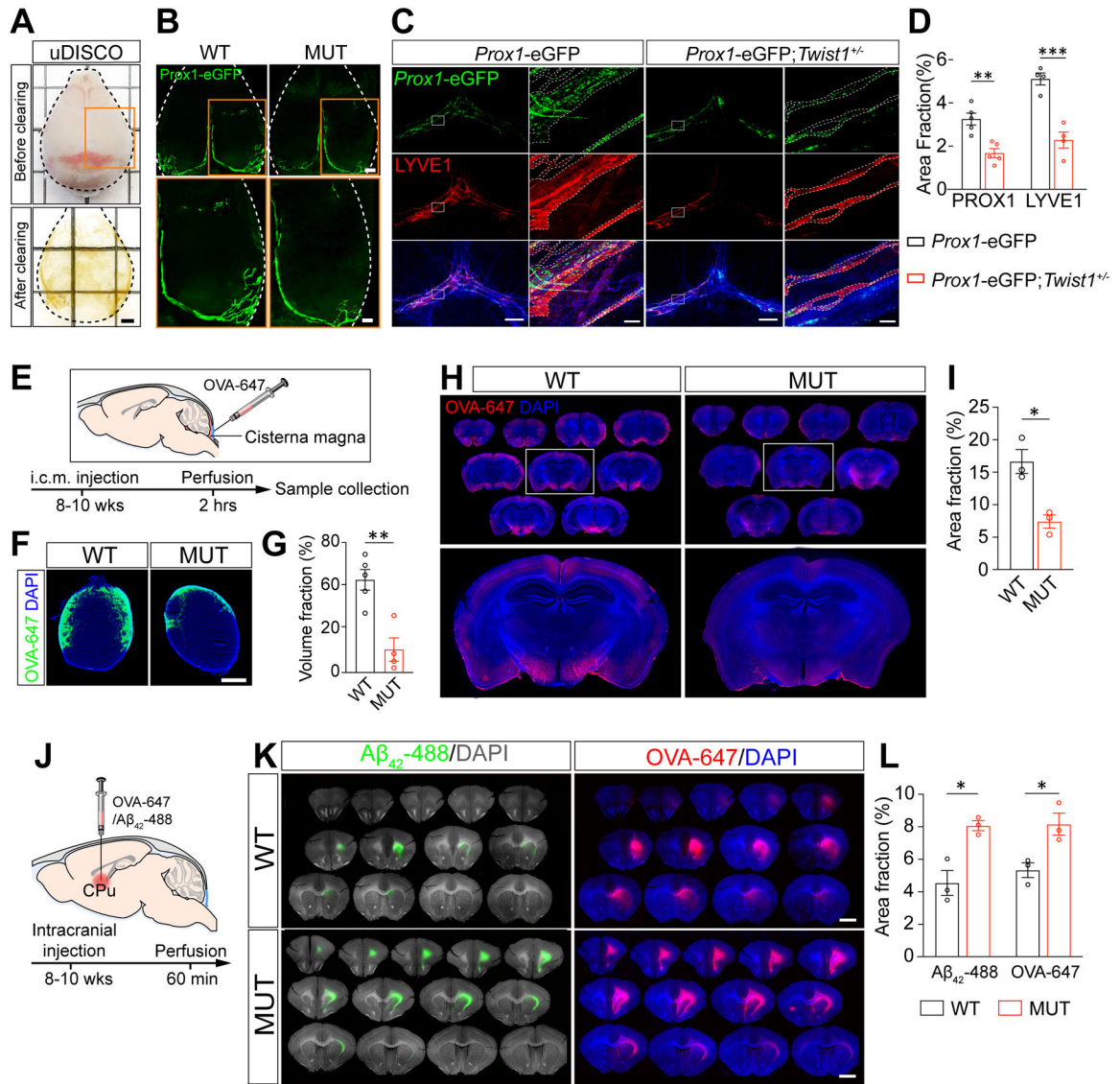


**Figure 1. *Twist1<sup>+/-</sup>* mice with craniosynostosis exhibit impaired meningeal lymphatics, CSF influx, and ISF efflux**

(A) Brightfield representative images of mouse head before (top) and after (bottom) uDISCO clearing. Scale bar, 2 mm. The mouse heads are outlined by dashed lines. The orange box indicates the zoomed imaging areas shown in (B).

(B) The low magnification light sheet microscopy images of a *Prox1-eGFP* mouse head after clearing. The skulls are outline by dashed lines, and the orange boxes indicate the zoomed imaging areas shown in the lower panel (B' and B''). Scale bars, 2 mm and 1 mm (inset).

(C) Representative images of meningeal whole-mount staining from *Prox1-eGFP* and *Prox1-eGFP; Twist1<sup>+/-</sup>* mice with antibody against LYVE1 (red). Nuclei were counterstained with DAPI (blue). The lymphatic vessels were outlined with dashed lines. Scale bar, 1 mm and 100 μm (inset).

- (D) Quantification of area fraction of PROX1<sup>+</sup> (left, *Prox1*-eGFP, n=5; *Prox1*-eGFP; *Twist1*<sup>+/-</sup>, n=5 mice) and LYVE1<sup>+</sup> (right, *Prox1*-eGFP, n=4; *Prox1*-eGFP; *Twist1*<sup>+/-</sup>, n=4 mice) lymphatic vessels.
- (E) Diagram showing that WT or MUT mice were injected (i.c.m.) with OVA-647, and after two hours, the brain and dCLNs samples were collected for analysis.
- (F) The representative images of dCLN sections collected from mice injected (i.c.m.) with OVA647 (green). Sections were counterstained with DAPI (blue). Scale bar, 200 μm.
- (G) Quantification of OVA-647<sup>+</sup> volume fraction of dCLNs (WT, n=5 and MUT, n=4 mice).
- (H) The representative images of brain coronal sections with OVA647 (red). Nuclei were counterstained with DAPI (blue). Scale bars, 2 mm and 1mm (inset).
- (I) Quantification of OVA-647<sup>+</sup> area fraction of brain sections (WT, n=3 and MUT, n=3 mice).
- (J) Diagrams showing that mouse corpus striatum (CPu) was intracranially injected with OVA-647 or Aβ<sub>42</sub>-488, and brain samples were collected after 60 min.
- (K) The representative images of brain coronal sections of mouse intracranially injected with Aβ<sub>42</sub>-488 (left panel) or OVA-647 (right panel). Nuclei were counterstained with DAPI. Scale bars, 2 mm.
- (L) Quantification of Aβ<sub>42</sub>-488<sup>+</sup> or OVA-647<sup>+</sup> area fraction of brain sections (WT, n=3 and MUT, n=3 mice). WT, wild-type mice; MUT, *Twist1*<sup>+/-</sup> mice with bilateral suture fusion. Data are mean ± SEM (d, g, i, and l). \*p<0.05, \*\*p<0.01, \*\*\*p<0.001 calculated by two-tailed unpaired t test.



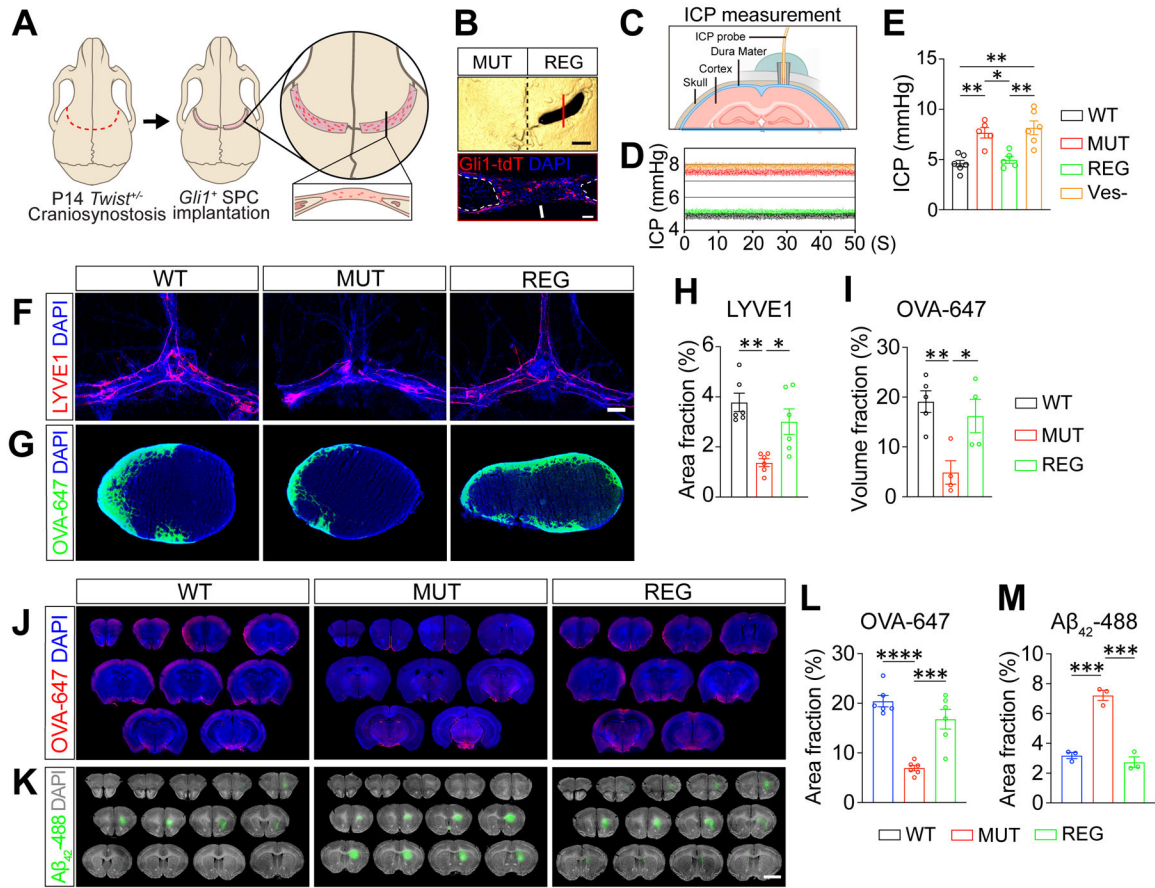


**Figure 2. Meningeal lymphatic defects are restored by SPC implantation in *Twist1*<sup>+/-</sup> mice**

(A) The schematic of *Gli1*<sup>+</sup> SPC implantation on *Twist1*<sup>+/-</sup> mouse with bilateral craniosynostosis.

(B) 3-D reconstructed microCT images of the calvaria of *Twist1*<sup>+/-</sup> mice with SPC implantation at one month post-surgery (upper panel) and immunofluorescent imaging of a coronal section of the *Gli1*<sup>+</sup> SPC implantation site (lower panel). White arrows indicate regenerating sutures, and white arrowheads indicate dura. Scale bars, 1 mm (upper panel) and 50  $\mu$ m (lower panel).

(C) A schematic of the ICP measurement setup.

(D and E) Representative ICP traces and quantification of ICP values (WT, n = 6; MUT, n = 5; REG, n=5; Ves- [Vessel ablation], n=6 mice).

(F) Representative images of meningeal whole-mount staining with antibody against LYVE1 (red). Nuclei were counterstained with DAPI (blue). Scale bar, 500  $\mu$ m.

(G) Representative images of dCLN sections of mice injected (i.c.m.) with OVA-647 (green). Nuclei were counterstained with DAPI (blue). Scale bar, 100  $\mu$ m.

(H) Quantification of area fraction of LYVE1<sup>+</sup> lymphatic vessels (WT, n=6; MUT, n=6; REG, n=6 mice).

(I) Quantification of OVA-647<sup>+</sup> volume fraction of dCLNs (WT, n=5; MUT, n=4; REG, n=4 mice).

(J) Representative images of brain coronal sections collected from mice injected (i.c.m.) with OVA-647 (red). Nuclei were counterstained with DAPI (Blue). Scale bar, 2 mm.

(K) The representative images of brain coronal sections collected from mice intracranially injected with A $\beta$ <sub>42</sub>-488. Nuclei were counterstained with DAPI (blue). Scale bar, 2 mm.

(L) Quantification of OVA-647<sup>+</sup> area fraction of brain sections (WT, n=6; MUT, n=6; REG, n=6 mice).

(M) Quantification of A $\beta$ <sub>42</sub>-488<sup>+</sup> area fraction of brain sections (WT, n=3; MUT, n=3; REG, n=3 mice).

Data are mean  $\pm$  SEM calculated by one-way ANOVA with Tukey post hoc tests. \*p<0.05, \*\*p<0.01, \*\*\*p<0.001, \*\*\*\*p<0.0001.

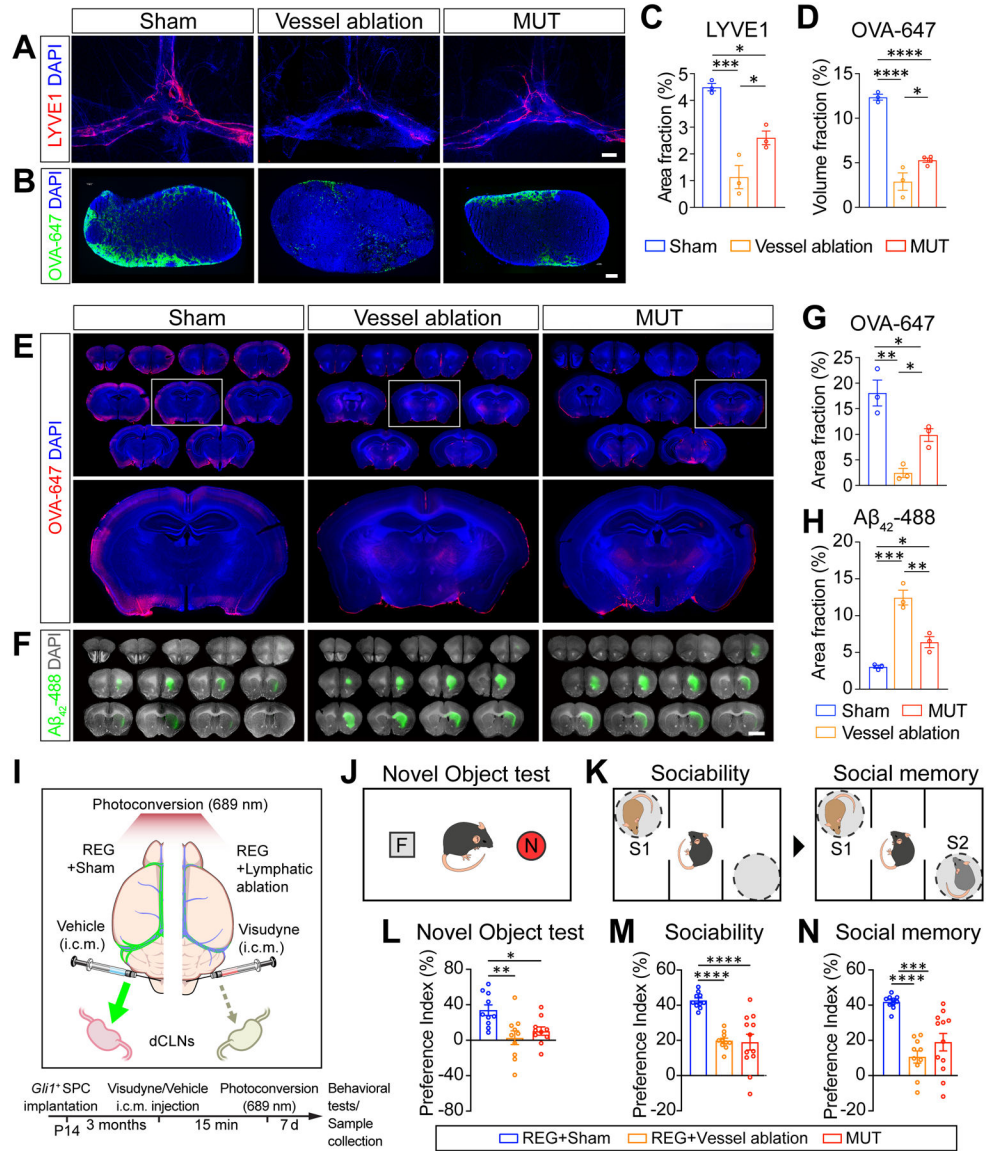


**Figure 3. Meningeal lymphatic vessel ablation blocks SPC implantation-mediated beneficial effects on neurocognitive function in *Twist1*<sup>+/-</sup> mice**

(A) Representative images of meningeal whole-mount staining with antibody against LYVE1 (red). Nuclei were counterstained with DAPI (blue). Scale bar, 500  $\mu$ m.

(B) Representative images of dCLN sections collected from mice injected (i.c.m.) with OVA-488. Nuclei were counterstained with DAPI. Scale bar, 100  $\mu$ m.

(C and D) Quantification of area fraction of LYVE1<sup>+</sup> lymphatic vessels and OVA-647<sup>+</sup> volume fraction of dCLNs (Sham, n=3; Vessel ablation, n=3; MUT, n=3 mice).

(E) The representative images of brain coronal sections collected from mice injected (i.c.m.) with OVA-647 (red). Nuclei were counterstained with DAPI (blue). Scale bar, 2 mm and 1 mm (inset).

(F) The representative images of brain coronal sections of mice intracranially injected with A $\beta$ <sub>42-488</sub> after 60 min. Sections were counterstained with DAPI. Scale bars, 2 mm.

(G) Quantification of OVA-647 area fraction (%).

(H) Quantification of A $\beta$ <sub>42-488</sub> area fraction (%).

(I) Experimental timeline: *Glil1*<sup>+</sup> SPC implantation at P14, 3 months later, i.c.m. injection (Visudyne/Vehicle) at P17, 15 min later, Photoconversion (689 nm) at P17, 7 days later, Behavioral tests/Sample collection.

(J) Novel Object test schematic.

(K) Sociability and Social memory test schematics.

(L, M, N) Behavioral results for Novel Object test, Sociability, and Social memory, respectively, showing Preference Index (%) for REG+Sham, REG+Vessel ablation, and MUT groups.

(G) Quantification of OVA-647<sup>+</sup> area fraction of brain sections after intra-cisterna magna injection (Sham, n=3; Vessel ablation, n=3; MUT, n=3 mice).

(H) Quantification of A $\beta$ <sub>42</sub>-488<sup>+</sup> (I) area fraction of brain sections collected from mice after intracranial injection (Sham, n=3; Vessel ablation, n=3; MUT, n=3 mice).

(I) Schematic of the lymphatic ablation performed on REG mice.

(J and K) Schematics of novel object (J) and three-chamber tests (K).

(L-N) Quantification of the preference index in the novel object test (L) as well as sociability (M) and social memory (N) in the three-chamber test (Sham, n=10; Vessel ablation, n=10; MUT, n=10 mice).

Data are mean  $\pm$  SEM calculated by one-way ANOVA with Tukey post hoc tests. \*p<0.05, \*\*p<0.01, \*\*\*p<0.001, \*\*\*\*p<0.0001.

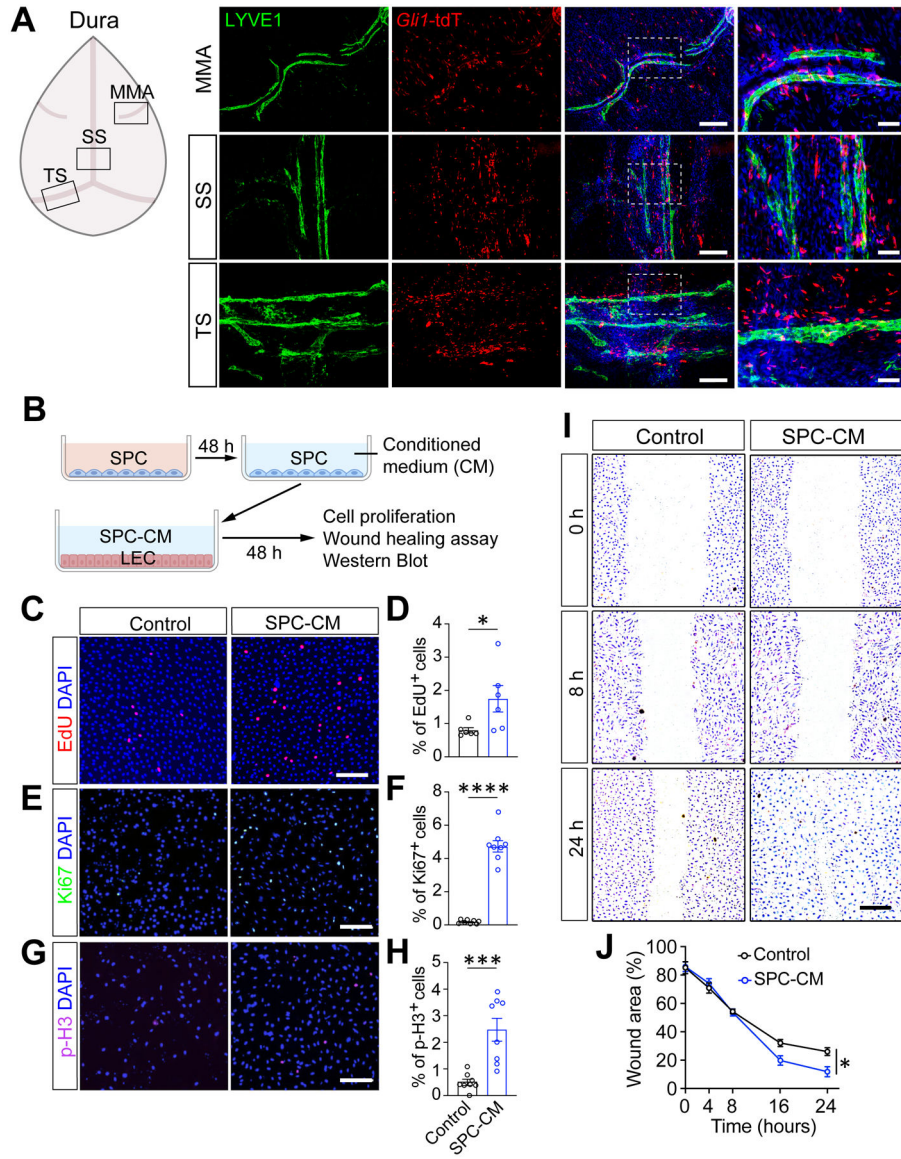


**Figure 4. SPCs promote lymphatic endothelial cell (LEC) proliferation and migration**  
 (A) Representative images of immunofluorescent staining of meningeal whole-mount staining with antibody against LYVE1 (green) focusing on the middle meningeal artery (MMA), superior sagittal sinus (SS), and transverse sinus (TS) regions. *Gli1*<sup>+</sup> cells were labeled with *Gli1-Cre<sup>ERT2</sup>;Rosa26-tdTomato* after Tamoxifen induction (*Gli1*-tdT, red). Scale bar, 500  $\mu$ m and 50  $\mu$ m (inset).  
 (B) Diagram showing that SPC conditioned medium (CM) was transferred into LECs followed by downstream assays.  
 (C, E, G) Representative images of EdU (C), Ki67 (E) and p-H3 (G) staining of the cultured LEC. Nuclei were stained with DAPI (blue). Scale bar, 50  $\mu$ m.  
 (D, F, H) Quantification of the percentage of EdU<sup>+</sup> (D), Ki67<sup>+</sup> (F) and p-H3<sup>+</sup> (H) cells out of total cells (Control, n=6–8; SPC-CM, n=6–8 mice).

(I) Representative images of cell scratch wound healing at the indicated time points after scratching. Scale bar, 200  $\mu\text{m}$ .

(J) Quantification of scratch-wound area monitored over time in LECs (Control, n=3; SPC-CM, n=3).

Data are mean  $\pm$  SEM calculated by two-tailed unpaired t test or one-way ANOVA with Tukey post hoc tests (\*p<0.05).

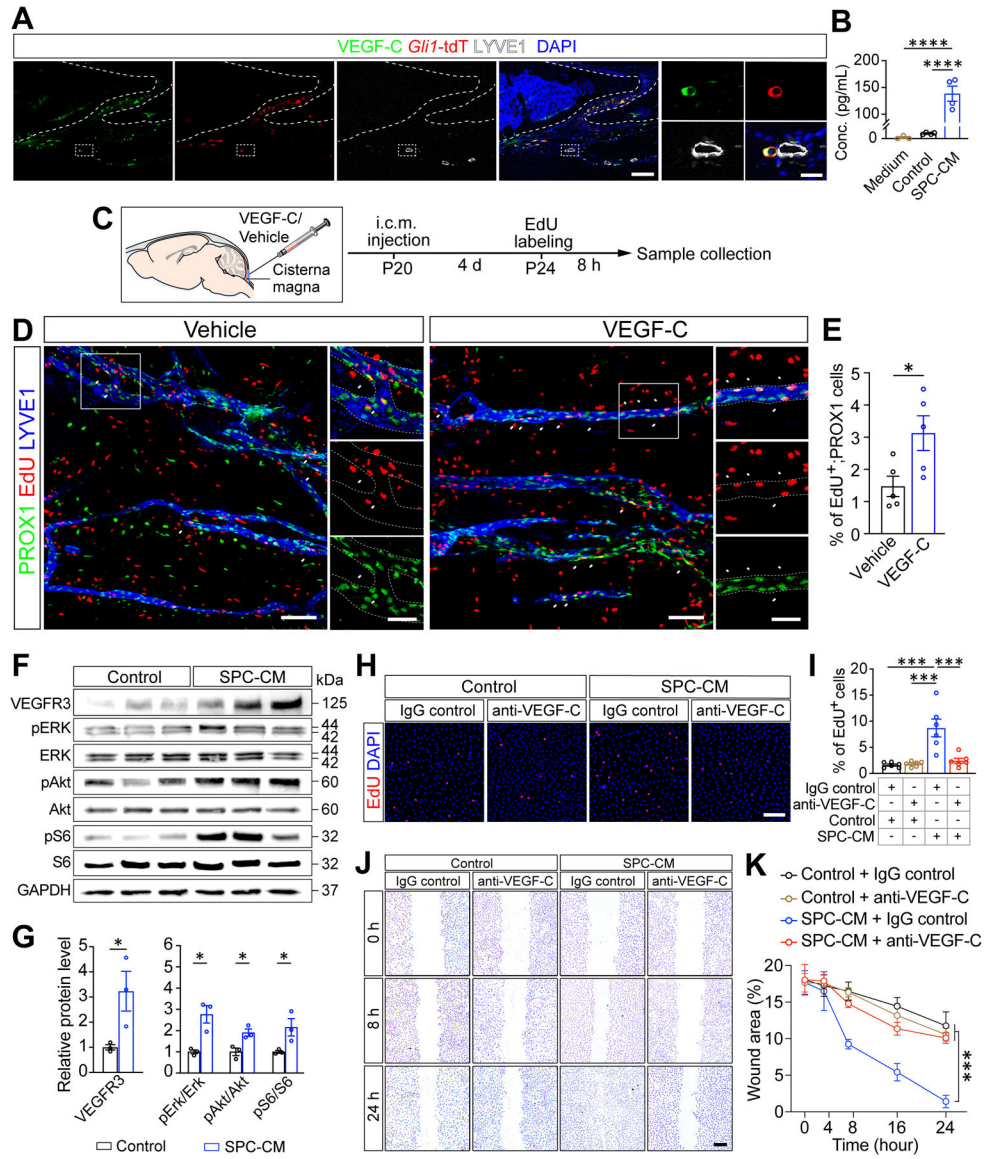


**Figure 5. VEGF-C signaling is essential for SPC-LEC interaction**

(A) Representative images of lambdoid suture staining with VEGF-C (green) and LYVE1 (white). *Gli1*<sup>+</sup> SPCs (red) were labeled with *Gli1-Cre<sup>ERT2</sup>; Rosa26-tdTomato* with Tamoxifen induction. Nuclei were counterstained with DAPI (blue). Scale bar, 100 μm and 20 μm (inset).

(B) ELISA measurement of VEGF-C concentrations in the LEC medium, hiPSC control, or SPC-CM (Medium, n= 3; Control, n=4; SPC-CM, n=4).

(C) Diagram showing that *Prox1*-eGFP<sup>+</sup> mice were injected (i.c.m.) with VEGF-C at P20, and after four days, EdU was injected (i.p.) and chased for eight hours before samples collection.

(D) Representative images of meningeal whole-mount staining with EdU (red) and LYVE1 (blue). Arrow heads indicate the EdU<sup>+</sup> cells co-labeled with Prox1-eGFP. The LYVE1<sup>+</sup>

lymphatic vessels were outlined with dashed lines in the zoomed area. Scale bar, 100  $\mu\text{m}$  and 50  $\mu\text{m}$  (inset).

(E) Quantification of the percentage of  $\text{EdU}^+;\text{Prox1}^+$  co-labeled cells to the total  $\text{Prox1-eGFP}^+$  cells. (Vehicle,  $n=5$ ; VEGF-C,  $n=5$  mice).

(F and G) Western blot analyses (F) and quantification of protein expression (G) in the LECs cultured with control or SPC-CM. The ratio of  $\text{pAkt}/\text{Akt}$ ,  $\text{pErk}/\text{Erk}$ , or  $\text{pS6}/\text{S6}$  of LECs co-cultured with control CM was set to 1, respectively (Control,  $n=3$ ; SPC-CM,  $n=3$ ).

(H) EdU staining of the LEC cultured in control or SPC-CM treated with anti-VEGF-C antibody or IgG isotype control. Nuclei were stained with DAPI (blue). Scale bar, 50  $\mu\text{m}$ .

(I) Quantification of the percentage of  $\text{EdU}^+$  cells out of total cells ( $n=6$  per group).

(J) Representative images of cell scratch wound healing at the indicated time points after scratching. Scale bar, 200  $\mu\text{m}$ .

(K) Quantification of scratch-wound area monitored over time in LECs with different treatments ( $n=3$  per group). Data are mean  $\pm$  SEM. \* $p<0.05$ , \*\*\* $p<0.001$ , \*\*\*\* $p<0.0001$ , calculated by one-way ANOVA with Tukey post hoc tests or two-tailed unpaired t test.



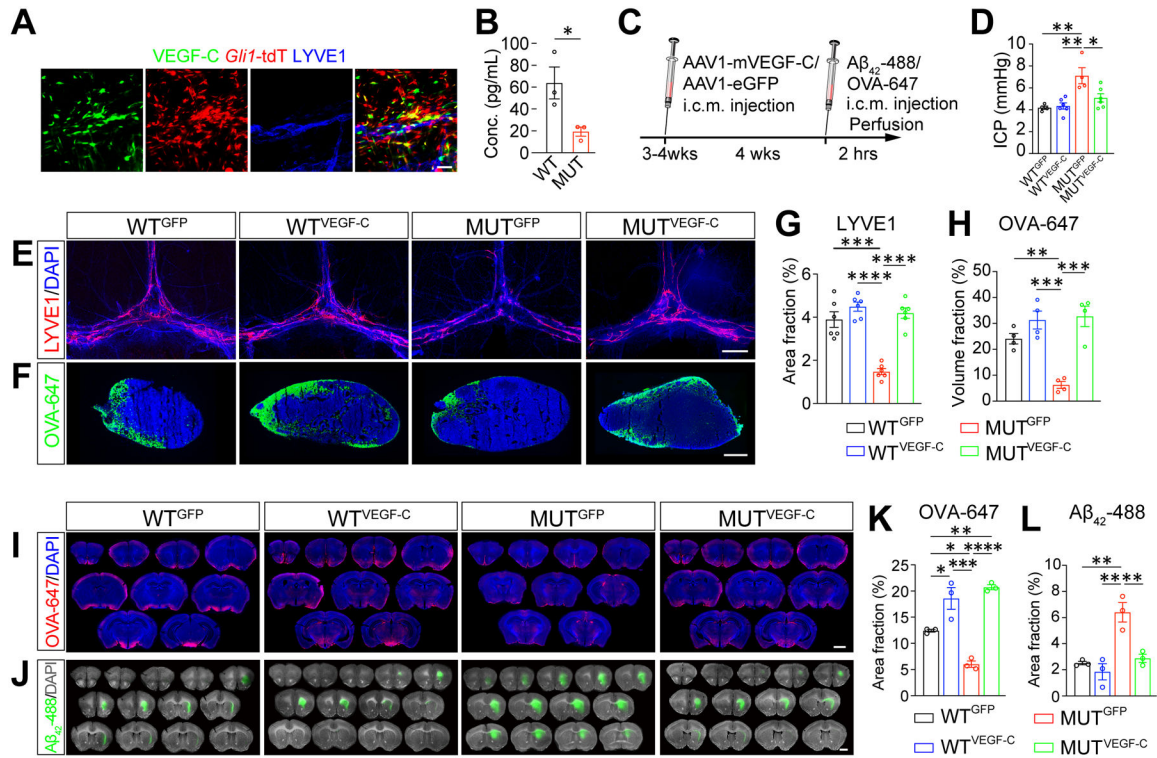


**Figure 6. VEGF-C treatment restores meningeal lymphatics, CSF influx, and ISF efflux in *Twist1*<sup>+/-</sup> mice with craniosynostosis**

(A) Representative images of meningeal whole-mount staining with antibodies against VEGF-C (green) and LYVE1 (blue). *Gli1*<sup>+</sup> SPCs (red) were labeled with *Gli1-Cre<sup>ERT2</sup>; Rosa26-tdTomato* with Tamoxifen induction. Scale bar, 50  $\mu$ m.

(B) ELISA measurement of VEGF-C concentrations in meningeal lysates (WT, n= 3; MUT, n=3).

(C) Diagrams showing that WT or MUT mice were injected (i.c.m.) with AAV1-eGFP or AAV1-VEGF-C, and 4 weeks later injected (i.c.m.) with A $\beta$ <sub>42</sub>-488 or OVA-647. Brain and dCLN samples were collected two hours after tracer injection.

(D) Quantification of the ICP (WT<sup>GFP</sup>, n=4; WT<sup>VEGF-C</sup>, n=6; MUT<sup>GFP</sup>, n=4; MUT<sup>VEGF-C</sup>, n=6 mice).

(E) Representative images of meningeal whole-mount staining with antibody against LYVE1 (red). Nuclei were counterstained with DAPI (blue). Scale bar, 500  $\mu$ m.

(F) The representative images of dCLN sections of mice injected (i.c.m.) with OVA-647. Sections were counterstained with DAPI. Scale bar, 100  $\mu$ m.

(G) Quantification of area fraction of LYVE1<sup>+</sup> lymphatic vessels (WT<sup>GFP</sup>, n=6; WT<sup>VEGF-C</sup>, n=6; MUT<sup>GFP</sup>, n=6; MUT<sup>VEGF-C</sup>, n=6 mice).

(H) Quantification of OVA-647<sup>+</sup> volume fraction of dCLNs (WT<sup>GFP</sup>, n=4; WT<sup>VEGF-C</sup>, n=4; MUT<sup>GFP</sup>, n=4; MUT<sup>VEGF-C</sup>, n=4 mice).

(I) Representative images of brain coronal sections of a mouse injected (i.c.m.) with OVA-647. Sections were counterstained with DAPI. Scale bar, 2 mm.

(J) The representative images of brain coronal sections collected from mice intracranially injected with A $\beta$ <sub>42</sub>-488 after 60 min. Nuclei were counterstained with DAPI (blue). Scale bar, 2 mm.

(K) Quantification of OVA-647<sup>+</sup> area fraction of brain sections (WT<sup>GFP</sup>, n=3; WT<sup>VEGF-C</sup>, n=3; MUT<sup>GFP</sup>, n=3; MUT<sup>VEGF-C</sup>, n=3 mice).

(L) Quantification of A $\beta$ <sub>42</sub>-488<sup>+</sup> area fraction of brain sections (WT<sup>GFP</sup>, n=3; WT<sup>VEGF-C</sup>, n=3; MUT<sup>GFP</sup>, n=3; MUT<sup>VEGF-C</sup>, n=3 mice).

Data are mean  $\pm$  SEM. \*p<0.05, \*\*p<0.01, \*\*\*p<0.001, \*\*\*\*p<0.0001, calculated by one-way ANOVA with Tukey post hoc tests.

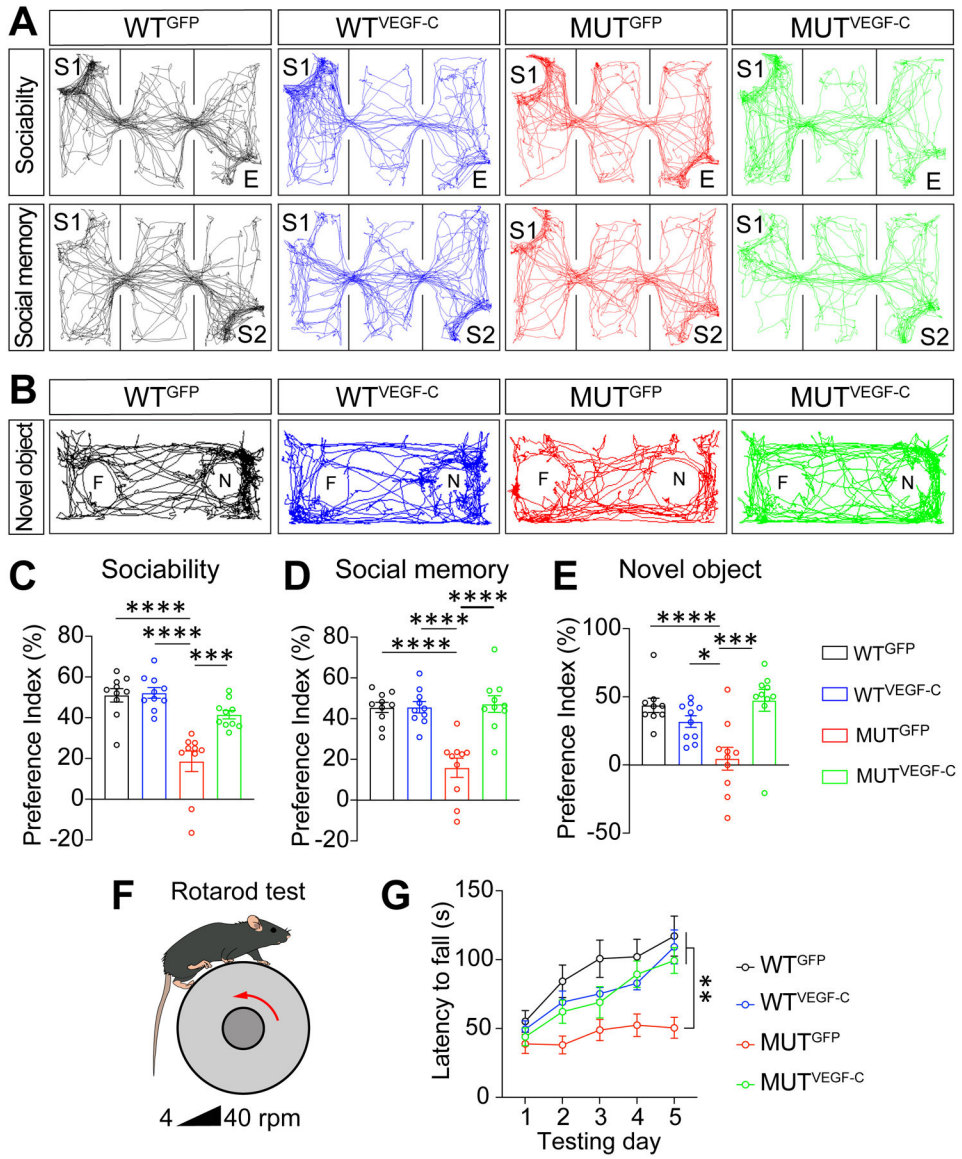


**Figure 7. VEGF-C treatment rescues the neurocognitive and motor behavior deficits of *Twist1*<sup>+/-</sup> mice with craniosynostosis**

(A) Representative animal tracks of sociability (upper panels) and social memory (lower panels) in the three-chamber test.

(B) Representative animal tracks of novel object test.

(C and D) Quantification of the preference index in sociability (C) and social memory (D) of three-chamber test (WT<sup>GFP</sup>, n=10; WT<sup>VEGF-C</sup>, n=10; MUT<sup>GFP</sup>, n=10; MUT<sup>VEGF-C</sup>, n=10 mice).

(E) Quantification of the preference index in the novel object test (WT<sup>GFP</sup>, n=10; WT<sup>VEGF-C</sup>, n=10; MUT<sup>GFP</sup>, n=10; MUT<sup>VEGF-C</sup>, n=10 mice).

(F) Schematics of the rotarod test.

(G) Rotarod performance scored as time (seconds) on the rotarod (WT<sup>GFP</sup>, n=10; WT<sup>VEGF-C</sup>, n=10; MUT<sup>GFP</sup>, n=10; MUT<sup>VEGF-C</sup>, n=10 mice).

Data are mean  $\pm$  SEM. \* $p < 0.05$ , \*\* $p < 0.01$ , \*\*\* $p < 0.001$ , \*\*\*\* $p < 0.0001$ , calculated by one-way ANOVA with Tukey post hoc tests.

Author Manuscript

Author Manuscript

Author Manuscript

Author Manuscript

## KEY RESOURCES TABLE

REAGENT or RESOURCE	SOURCE	IDENTIFIER
Antibodies		
Rabbit polyclonal anti-Sp7	Abcam	ab209484
Rat anti-LYVE1	Invitrogen	14-0443-82
Rabbit anti-VEGF-C	NovusBio	NB110-61022
Rabbit anti-Ki67	Abcam	ab15580
Goat anti-LYVE1	R&D systems	AF2089
Rabbit anti-aSMA	Abcam	ab5694
Rabbit anti-NG2	Sigma-Aldrich	AB5320
Goat anti-PROX1	R&D systems	AF2737
Goat anti-VEGFR3	R&D systems	AF743
Mouse Anti-Human VEGFR-3/FLT-4	ReliaTech	101-M36
Rabbit anti-Phospho-p44/42 MAPK (Erk1/2) (Thr202/Tyr204)	Cell Signaling technology	4370
Rabbit anti-p44/42 MAPK (Erk1/2)	Cell Signaling technology	4695
Rabbit anti-Phospho-Akt (Ser473)	Cell Signaling technology	4060
Rabbit anti-Akt	Cell Signaling technology	9272
Rabbit anti-Phospho-S6 Ribosomal Protein (Ser240/244)	Cell Signaling technology	35708
Rabbit anti-S6 Ribosomal Protein	Cell Signaling technology	2217
Rabbit anti-GAPDH	Cell Signaling technology	2118
Goat anti-Rabbit IgG (H+L) Cross-Adsorbed Secondary Antibody, Alexa Fluor™ 568	Thermo Fisher Scientific	A-11011
Goat anti-Rat IgG (H+L) Cross-Adsorbed Secondary Antibody, Alexa Fluor™ 647	Thermo Fisher Scientific	A-21247
Donkey anti-Goat IgG (H+L) Cross-Adsorbed Secondary Antibody, Alexa Fluor™ 488	Thermo Fisher Scientific	A-11055
Goat Anti-Rabbit (GAR)-HRP Conjugate	Biorad	1705046
Goat Anti-Mouse (GAM)-HRP Conjugate	Biorad	1705047
Bacterial and virus strains		
AAV1-CMV-eGFP	Vector Biolabs	7002
AAV1-CMV-mVEGF-C	Vector Biolabs	AAV-275994
TWIST1 shRNA lentiviral particles	Santa Cruz Biotechnology	sc-38604-V
Control shRNA lentiviral particles-A	Santa Cruz Biotechnology	sc-108080
Chemicals, peptides, and recombinant proteins		
Methacrylic anhydride	Sigma-Aldrich	276685
Gelatin	Sigma-Aldrich	69391
Matrigel	Corning	8015323
Collagen I	GIBCO	A10483-01
Lithium phenyl-2, 4, 6-trimethylbenzoylphosphinate	TOCRIS	6146
TrypLE Express Enzyme (1X)	GIBCO	1897328
MEM $\alpha$ , nucleosides	GIBCO	2065542

REAGENT or RESOURCE	SOURCE	IDENTIFIER
Fetal Bovine Serum	GIBCO	2100184
2-mercaptoethanol	GIBCO	2090354
Penicillin-Streptomycin (10000 U/mL)	GIBCO	2019321
EDTA	Sigma-Aldrich	E9884
Tert-Butanol	Sigma-Aldrich	360538
Benzyl alcohol	Sigma-Aldrich	402834
Benzyl benzoate	Sigma-Aldrich	B6630
Diphenyl ether	Sigma-Aldrich	240834
Alexa Fluor 647-conjugated OVA	Thermo Fisher Scientific	O34784
Beta-Amyloid (1–42), HiLyte™ Fluor 488	AnaSpec	AS-60479-01
Visudyne	APExBIO	A8327
TRIzol™ Reagent	Thermo Fisher Scientific	15596026
Tamoxifen	Sigma-Aldrich	T5648
Paraformaldehyde, 4% in PBS	Thermo Fisher Scientific	J61899-AP
D-(+)-Sucrose, Ultrapure DNase-, RNase-free	VWR	97061-432
Tissue-Plus O.C.T. compound	Thermo Fisher Scientific	23-730-571
Sodium azide	Sigma-Aldrich	S2002
Heparin sodium salt	Sigma-Aldrich	H3149
Polyethylenimine	Polyscience	23966-1
Polybrene	Sigma-Aldrich	R-1003-G
Salt-activated nuclease	ArcticZymes	10977-023
OptiPrep - Density Gradient Media (Iodixanol)	Cosmo Bio USA	AXS-1114542-5
Recombinant human VEGF-C (Cys156Ser) protein	R&D systems	752-VC-025/CF
Artificial CSF	Tocris Bioscience	3525
Rat IgG Isotype Control	Invitrogen	31933
Rabbit IgG Isotype Control	Proteintech	30000-0-AP
VECTASHIELD® Antifade Mounting Medium	Vector Laboratories	H-1000
RIPA buffer	Cell Signaling technology	9806
Protease Inhibitor Cocktails	Thermo Fisher Scientific	1861278
PMSF Protease Inhibitor	Thermo Fisher Scientific	36978
Cresyl Violet acetate	Sigma-Aldrich	C5042
5-ethynyl-2'-deoxyuridine (EdU)	Thermo Fisher Scientific	A10044
Critical commercial assays		
StemPro Osteogenesis Differentiation Kit	Gibco	A1007201
BCA protein assay kit	Thermo Fisher Scientific	23227
Azure 300	Azure Biosystems	Azure 300
EGM™ Endothelial Cell Growth Medium BulletKit™	Lonza	CC-3124
MCDB131 media	Sigma-Aldrich	M8537

REAGENT or RESOURCE	SOURCE	IDENTIFIER
Click-iT™ RNA Alexa Fluor™ 594 Imaging Kit	Thermo Fisher Scientific	C10330
RNAscope Multiplex Fluorescent v2 kit	Advanced Cell Diagnostics	323100
TSA Plus Cyanine 5 system	PerkinElmer	NEL745001KT
SuperScript™ VILO™ cDNA Synthesis Kit	Thermo Fisher Scientific	11754050
SsoAdvanced™ Universal SYBR® Green Supermix	Biorad	1725271
Deposited data		
Experimental models: Cell lines		
HEK293T cells	ATCC	CRL-3216
Human primary lymphatic endothelial cells	Hirakawa et al. <sup>34</sup>	N/A
<i>Gli1</i> <sup>+</sup> cells	This paper	N/A
Experimental models: Organisms/strains		
Mouse: C57BL/6J	The Jackson Laboratory	000664
Mouse: <i>Gli1</i> -CreERT2 ( <i>Gli1</i> <sup>tm3(cre/ERT2)Alj/J</sup> )	The Jackson Laboratory	007913
Mouse: B6;129S6-Gt(ROSA)26Sor <sup>tm9(CAG-tdTomato)Hze/J</sup>	The Jackson Laboratory	007905
Mouse: Twist-null (B6;129S-Twist1 <sup>tm1Bhr/J</sup> )	The Jackson Laboratory	002221
Mouse: Prox1-GFP	Choi et al. <sup>24</sup>	N/A
Oligonucleotides		
RNAscope™ Probe- Mm-Twist1-O1-C1	Advanced Cell Diagnostics	1266861
RNAscope™ Probe- Mm-Col1a1	Advanced Cell Diagnostics	319371
qPCR primers: <i>Twist1</i> forward: GGACAAGCTGAGCAAGATTCA;	Integrated DNA Technologies	N/A
qPCR primers: <i>Twist1</i> reverse: GGACAAGCTGAGCAAGATTCA	Integrated DNA Technologies	N/A
qPCR primers: <i>Actb</i> forward: TCCGGCACTACCGAGTTATC	Integrated DNA Technologies	N/A
qPCR primers: <i>Actb</i> reverse: GATCCGGTGTAGCAGATCGC	Integrated DNA Technologies	N/A
qPCR primers: WPRE forward: GGCTGTTGGGCACTGACAAT	Invitrogen	N/A
qPCR primers: WPRE reverse: CCGAAGGGACGTAGCAGAAG	Invitrogen	N/A
Recombinant DNA		
psubCMV-mVEGF-D-WPRE	Kari Alitalo Lab	Addgene, #119226
pAAV2/1	James M. Wilson Lab	Addgene, #112862
pAdDeltaF6	James M. Wilson Lab	Addgene, #112867
Software and algorithms		
Evolution	<a href="https://fiso.com/en/product-software-downloads/">https://fiso.com/en/product-software-downloads/</a>	N/A

REAGENT or RESOURCE	SOURCE	IDENTIFIER
Smart v3.0	<a href="https://www.harvardapparatus.com/smart-video-tracking-system.html">https://www.harvardapparatus.com/smart-video-tracking-system.html</a>	76-0696
Imaris 9	<a href="https://imaris.oxinst.com/">https://imaris.oxinst.com/</a>	N/A
ImageJ	<a href="https://fiji.sc/">https://fiji.sc/</a>	N/A
Leica Application Suite X	<a href="https://www.leica-microsystems.com/products/microscope-software/p/leica-las-x-ls/">https://www.leica-microsystems.com/products/microscope-software/p/leica-las-x-ls/</a>	N/A
Prism 8	<a href="https://www.graphpad.com/scientific-software/prism/">https://www.graphpad.com/scientific-software/prism/</a>	N/A

Author Manuscript

Author Manuscript

Author Manuscript

Author Manuscript